

A Spectro-photometric Analysis of Cool White Dwarfs in the Gaia and Pan-STARRS Footprint

Alexandre Caron¹, P. Bergeron¹, Simon Blouin², and S. K. Leggett³

¹Département de Physique, Université de Montréal, C.P. 6128, Succ. Centre-Ville, Montréal, QC H3C 3J7, Canada

²Department of Physics and Astronomy, University of Victoria, Victoria, BC V8W 2Y2, Canada

³Gemini Observatory/NSF's NOIRLab, 670 N. A'ohoku Place, Hilo, HI 96720, USA

16 December 2022

ABSTRACT

We present a spectro-photometric analysis of 2880 cool white dwarfs within 100 pc of the Sun and cooler than $T_{\text{eff}} \sim 10,000$ K, with *grizy* Pan-STARRS photometry and Gaia trigonometric parallaxes available. We also supplement our data sets with near-infrared *JHK* photometry, when available, which is shown to be essential for interpreting the coolest white dwarfs in our sample. We perform a detailed analysis of each individual object using state-of-the-art model atmospheres appropriate for each spectral type including DA, DC, DQ, DZ, He-rich DA, and the so-called IR-faint white dwarfs. We discuss the temperature and mass distributions of each subsample, as well as revisit the spectral evolution of cool white dwarfs. We find little evidence in our sample for the transformation of a significant fraction of DA stars into He-atmosphere white dwarfs through the process of convective mixing between $T_{\text{eff}} = 10,000$ K and ~ 6500 K, although the situation changes drastically in the range $T_{\text{eff}} = 6500\text{--}5500$ K where the fraction of He-atmosphere white dwarfs reaches $\sim 45\%$. However, we also provide strong evidence that at even cooler temperatures ($T_{\text{eff}} \lesssim 5200$ K), most DC white dwarfs have H atmospheres. We discuss a possible mechanism to account for this sudden transformation from He- to H-atmosphere white dwarfs involving the onset of crystallization and the occurrence of magnetism. Finally, we also argue that DQ, DZ, and DC white dwarfs may form a more homogeneous population than previously believed.

Key words: stars: abundances – stars: evolution – stars: fundamental parameters – stars: luminosity function, mass function – white dwarfs

1 INTRODUCTION

The determination of the fundamental parameters of white dwarfs – effective temperature, radius, mass, surface gravity, chemical composition, and cooling age – is of utmost importance for our understanding of their global properties such as their temperature and mass distributions, and their spectral evolution as well. The use of white dwarfs as cosmochronometers, whether it is through the study of their luminosity function or just by finding the oldest members of a given population, also requires precise and accurate stellar parameters. There are basically two main techniques that have been applied to large sample of white dwarfs. The first one is the spectroscopic technique (Bergeron et al. 1992; Liebert et al. 2005; Koester et al. 2009; Gianninas et al. 2011; Tremblay et al. 2011), where optical spectra are compared to the predictions of detailed synthetic spectra to measure both the effective temperature, T_{eff} , and surface gravity, $\log g$ (and in some instances the abundance of trace elements), which are then converted into stellar mass using evolutionary models. The second technique is the photometric technique (Bergeron et al. 1997; Hollands et al. 2018; Tremblay et al. 2019a), where magnitudes are converted into average fluxes in several bandpasses, and compared to the prediction of model atmospheres, synthetic photometry in this case (Holberg & Bergeron 2006). Here, T_{eff} and the solid angle

$\pi(R/D)^2$ are the fitted parameters, where R is the stellar radius and D is the distance from Earth, which can be obtained from trigonometric parallax measurements.

Over the years, we have observed a constant evolution of observational data and theoretical models, with sometimes one aspect being ahead of the other. For instance, Bergeron et al. (1992) applied the spectroscopic technique to a sample of only 129 DA stars using model spectra that included the Hummer-Mihalas occupation probability formalism (Hummer & Mihalas 1988), which allowed for the first time realistic quantitative measurements of the atmospheric parameters. All observed spectra in those days were secured individually using single-slit spectroscopy. In more recent years, the Sloan Digital Sky Survey (SDSS), with its very efficient multi-fiber spectrograph, has revolutionized the field by providing tens of thousands white dwarf spectra, and uncovered several new spectral classes (Kleinman et al. 2013; Kepler et al. 2019). But detailed analyses of such large white dwarf samples has also revealed problems with the microphysics of model spectra (see, e.g., Genest-Beaulieu & Bergeron 2019a).

Similarly, Bergeron et al. (1997, 2001) applied the photometric technique to over 200 white dwarfs by measuring optical *BVRI* and near-infrared *JHK* photometry of individual stars, with only 152 with trigonometric parallax measurements available. Their model atmo-

spheres relied on pure hydrogen, pure helium, or mixed H/He compositions, which could lead to large uncertainties when applied to DQ and DZ white dwarfs. Dufour et al. (2005, 2007) analysed only years later the same DQ and DZ stars using detailed model atmospheres including traces of carbon and heavier elements. Now the amount of photometric and astrometric data required to apply the photometric technique has sky rocketed, thanks to large photometric surveys such as the SDSS and Pan-STARRS (Panoramic Survey Telescope And Rapid Response System; Chambers et al. 2016, Tonry et al. 2012), and most importantly the Gaia astrometric mission, which provided precise astrometric and photometric data for $\sim 260,000$ high-confidence white dwarf candidates (Gentile Fusillo et al. 2019, 2021). Such large data sets have recently been equally matched by improvements with model atmospheres, in particular at the cool end of the white dwarf sequence where high atmospheric densities are reached (Kowalski & Saumon 2006; Kowalski et al. 2007; Blouin et al. 2017, 2018a,b; Blouin & Dufour 2019). In parallel, similar efforts have been put forward to secure spectroscopic observations of white dwarf candidates in the Gaia survey (Kilic et al. 2020; Tremblay et al. 2020; O’Brien et al. 2022).

Given these large amounts of data, it is common to attack the problem by plowing through the photometric data sets and use the photometric technique by making sound assumptions regarding the atmospheric composition of each white dwarf in the sample (see, e.g., Bergeron et al. 2019, López-Sanjuan et al. 2022). However, there are some limitations to this approach since ideally, one should perform a tailored model atmosphere analysis of each individual object in the sample, including also spectroscopic data. This is particularly important for DQ and DZ stars since the presence of heavy elements in the photospheric regions is known to affect the global atmospheric structure and thus the derived atmospheric parameters (Dufour et al. 2005, 2007).

In this paper, we present such a detailed spectro-photometric analysis of all spectroscopically identified white dwarfs within 100 pc from the Sun, based on Gaia distances. We restrict our analysis to objects below $T_{\text{eff}} \sim 10,000$ K and use a homogeneous set of model atmospheres to study the DA, DC, DQ, DZ, He-rich DA, and the so-called IR-faint white dwarfs present in our sample. Our secondary goal is to improve our global effort to provide the best physical parameters of each white dwarf in the Montreal White Dwarf Database¹ (MWDD; Dufour et al. 2017).

We present in Section 2 the selection of our white dwarf sample and observational data sets, which are then analysed in Section 3 using model atmospheres and fitting techniques appropriate for each spectral type. We present selected results in Section 4 including a discussion of the spectral evolution of white dwarfs. Our conclusions follow in Section 5.

2 OBSERVATIONAL DATA

2.1 Sample Selection

We first selected all white dwarfs – spectroscopically confirmed as well as candidates – found in the MWDD within 100 pc from the Sun. We chose this distance limit to avoid problems related to interstellar reddening. As specified in the MWDD, the white dwarf candidates in the 100 pc sample are selected from the Gaia Data Release 2 (DR2, Gaia Collaboration et al. 2018b), allowing for the error on the parallax measurement; we also included 27 objects for

which the parallax measurements became available only in the Gaia Early Data Release 3 (EDR3; Gaia Collaboration et al. 2022)². The recommendations described in Lindegren et al. (2018) were used to remove non-Gaussian outliers in colours and absolute magnitudes, and the sample was limited to objects with $> 10\sigma$ significant parallax (Bergeron et al. 2019, Kilic et al. 2020, MWDD). A cut in the $(G_{\text{BP}} - G_{\text{RP}}) - M_G$ plane was then performed to select the white dwarf candidates (see also Kilic et al. 2020). Finally, we retained only objects with Pan-STARRS *grizy* photometry measured in at least 3 photometric bands, and restricted our analysis to white dwarfs cooler than $T_{\text{eff}} \sim 10,000$ K based on the photometric analyses described below.

Considering all the selection criteria, we end up with 8238 objects in our sample, including 2880 spectroscopically confirmed white dwarfs and 5358 white dwarf candidates.

2.2 Photometric and Spectroscopic Data

As mentioned above, we make use of the Pan-STARRS *grizy* photometry available in the MWDD, although in the course of our analysis, we discovered several erroneous, or simply missing, photometric data sets in the MWDD, which have been corrected since. We also supplement our *grizy* data sets with SDSS *u* magnitudes, which represent a powerful diagnostic for the study of cool white dwarfs, as demonstrated in Kilic et al. (2020). When the Pan-STARRS photometry appeared in error, we rely instead on the SDSS *griz* photometry. Finally, 7 white dwarfs in our sample are brighter than $g = 13.5$ (e.g., WD 0135-052 = EG 11 = L870-2 with $g = 12.95$) and the magnitudes are obviously saturated, in agreement with the limits provided in Magnier et al. (2013). For these objects we adopt instead the optical *BVRI* photometry available in the MWDD.

Bergeron et al. (1997, 2001) discussed at length the importance of using near-infrared *JHK* photometry for the analysis of cool white dwarfs. Blouin et al. (2019), for instance, revisited the spectral evolution of cool white dwarfs by restricting their sample only to objects with infrared photometry available in the Two Micron Sky Survey (2MASS). Here we go further by including all *JHK* photometry published in the literature, and also matched the spectroscopically confirmed white dwarf sample to the near-infrared photometric catalogs provided by 2MASS, the Tenth Data Release of the UKIRT Infrared Deep Sky Survey (UKIDSS), the UKIRT Hemisphere Survey (UHS) JBand Data Release, and the Visible and Infrared Survey Telescope for Astronomy (VISTA) public survey (see also Leggett et al. 2018). We end up with about 92% of the objects in our sample having *JHK* photometry in at least one band (usually *J*), 61% in at least two bands, and 51% in all three.

Optical spectra are also used in our model atmosphere analysis to constrain the atmospheric composition of the objects in our sample in the case of DA and DC stars, or to measure the carbon and metal abundances in the case of DQ and DZ stars, respectively. We rely here on the spectra available in the MWDD, which have been secured from various sources, but mostly from the SDSS. For some objects without spectra, we rely on the spectral types provided in the MWDD, which come essentially from Simbad. Some of these spectral types can be confirmed from the spectra published in the literature (see, e.g., Kawka et al. 2007), while others have published spectral types without any actual spectra being displayed, and these

² We estimated that the parallax zero-point corrections proposed by Lindegren et al. (2021) are of the order of 0.010 mas for our sample and were thus not applied.

¹ <http://montrealwhitedwarfdatabase.org/>

should be considered more uncertain. Also, in the course of our analysis, we revised some of the published spectral types, and these are indicated in the results presented below.

We summarize in Table 1 the observational data used in our analysis, where we provide for each object the given J name based on Gaia coordinates, Gaia ID (DR2; if not available the EDR3 is given and marked by a star symbol in Table 1), spectral type, trigonometric parallax measurement (ϖ), SDSS u photometry, Pan-STARRS $grizy$ photometry, and near-infrared JHK photometry. The spectral types followed by an asterisk symbol correspond to newly assigned types based on our analysis.

2.3 Colour-Magnitude Diagrams

Before proceeding with a detailed model atmosphere analysis of the observational material described above, it is worth examining a few colour-magnitude diagrams. Figure 1 shows the M_g versus $(g - z)$ colour-magnitude diagram built from Pan-STARRS photometry. White dwarfs of various spectral types are identified by different colours. Also superposed are cooling sequences for $0.6 M_\odot$ CO-core models with pure H and pure He compositions, as well as mixed compositions of $\log H/He = -5$ and -2 . Here and in the remainder of this paper, we rely on the evolutionary models described in Bédard et al. (2020) with C/O cores, $q(He) \equiv \log M_{He}/M_\star = 10^{-2}$ and $q(H) = 10^{-4}$, which are representative of H-atmosphere white dwarfs, and $q(He) = 10^{-2}$ and $q(H) = 10^{-10}$, which are representative of He-atmosphere white dwarfs. As discussed at length by Bergeron et al. (2019), a trace of hydrogen is required to match the observed sequence of He-rich objects in Figure 1 with $0.6 M_\odot$ models, in particular the DC and DZ white dwarfs. Such a trace of hydrogen is predicted by the transformation of DA stars into He-rich white dwarfs through convective mixing (see Figure 4 of Bédard et al. 2022a). Note in particular how the DZ stars overlap nicely with the DC white dwarfs in this colour-magnitude diagram.

The pure H sequence in Figure 1 follows perfectly the observed DA sequence, except at the faint end where the predicted magnitudes fall below the observed sequence. The problem is exacerbated at even lower luminosities where the observed DC sequence – presumably the extension of the DA sequence at lower temperatures when $H\alpha$ disappears – lies significantly above the $0.6 M_\odot$ pure H sequence. The problem is even worse if one assumes a pure He or mixed H/He compositions, as seen in Figure 1. This discrepancy between observed and predicted colours translates into low inferred masses at low luminosities when the photometric method is applied to this data set, as illustrated in Figure 12 of Bergeron et al. (2019), and even more so when assuming He-rich atmospheres. The origin of this problem is still unknown.

Also observed at higher luminosities in Figure 1 is the crystallization sequence (the so-called Q-branch) composed of a pile up of massive DA stars caused by the release of latent heat and chemical fractionation, which decrease the cooling rate of a white dwarf (Tremblay et al. 2019b). In this particular color-magnitude diagram, this sequence of massive DA stars is well separated from the normal $\sim 0.6 M_\odot$ DA white dwarfs.

Also of interest in Figure 1 is the small number of white dwarfs at faint luminosities in the region where He-rich objects should be located according to the model predictions. It is precisely this dearth of cool DC stars at low luminosities with colours consistent with pure helium compositions that led Kowalski & Saumon (2006) to conclude that most cool, DC white dwarfs must have pure H atmospheres. We come back to this point below. Perhaps even more important is the existence of two distinct DC sequences, one at very

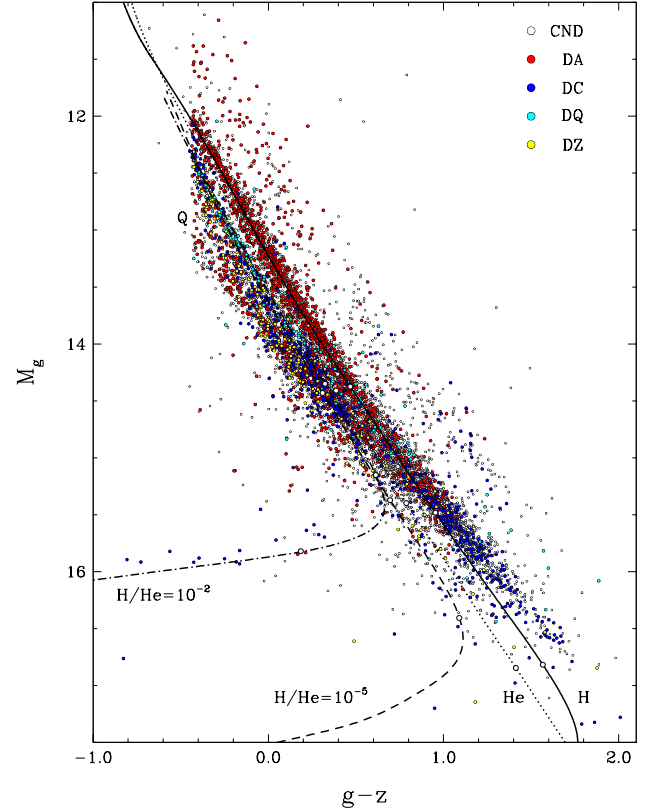


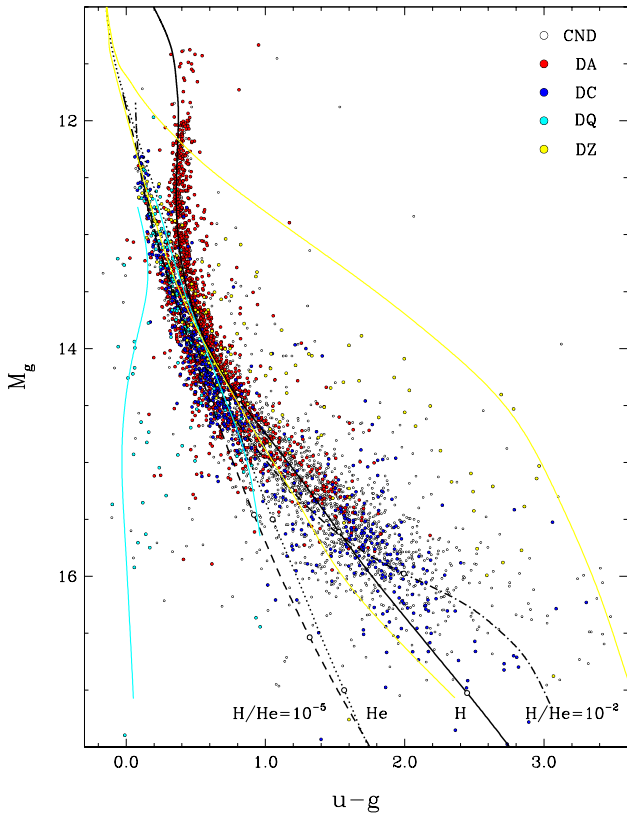
Figure 1. Pan-STARRS M_g versus $(g - z)$ colour-magnitude diagram for the 100 pc sample drawn from the MWDD. The various spectral types as well as the white dwarf candidates (CND) are identified with different colour symbols indicated in the legend. The various curves correspond to cooling sequences for $0.6 M_\odot$ CO-core models with pure H, pure He, $\log H/He = -5$ and -2 atmospheric compositions; white circles on each curve indicate $T_{\text{eff}} = 6000$ K, 5000 K, and 4000 K. The crystallization sequence (the so-called Q-branch), composed of a pile up of massive DA stars, is also indicated by the letter Q.

low luminosities that appears as the extension of the DA sequence, but also a more luminous DC sequence, which terminates abruptly at $T_{\text{eff}} \sim 5200$ K according to the theoretical models displayed in Figure 1. Moreover, there are very few DC stars connecting these two DC sequences. We can also see a deficiency of spectroscopically confirmed white dwarfs near $M_g \sim 15$ and $(g - z) \sim 0.7$, but this appears to be an observational bias since there are plenty of white dwarf candidates (CND) in the same region.

Figure 2 shows the M_g versus $(u - g)$ colour-magnitude diagram built from the subsample of objects with SDSS photometry (SDSS g here). In this particular diagram, the DA and DC sequences are well-separated at high luminosities as a result of the Balmer jump present in H atmospheres. The $0.6 M_\odot$ pure H, pure He, and mixed H/He sequences are also reproduced in this figure, but in addition we show $0.6 M_\odot$ white dwarf models for DQ stars with $\log C/He = -7.5$ and 5.0 , and for DZ stars with $\log Ca/He = -11.5$ and -7.0 , which correspond roughly to values that bracket the abundances measured for each spectral type in this temperature range (see Figures 8 and 12 of Coutu et al. 2019). Interestingly, the effect on the predicted colours goes in the opposite direction when traces of carbon in DC stars and metals in DZ stars are gradually increased, in agreement with the location of these white dwarfs in this particular colour-magnitude diagram. Note again here the lack of He-atmosphere white dwarfs at

Table 1. Observational Data. The spectral types followed by an asterisk symbol correspond to newly assigned types based on our analysis. This table, including uncertainties, is available in its entirety in machine-readable form as well as a pdf file.

Name	Gaia ID (DR2/EDR3*)	Sp Type	ϖ (mas)	u	g	r	i	z	y	J	H	K
J0000+0132	2738626591386423424	DA	14.95	16.65	16.23	16.34	16.48	16.64	16.75	16.23	16.14	16.24
J0000+1906	2774195552027050880	DC	9.800	23.29	20.32	19.73	19.52	19.43	19.34	18.65
J0001+3237	2874216647336589568	DC	10.15	20.42	19.49	19.16	19.06	19.04	19.01	18.32
J0001+3559	2877080497170502144	DC*	11.66	20.04	19.03	18.85	18.83	18.58	18.45	17.81
J0001-1111	2422442334689173376	DC	13.51	19.09	18.48	18.28	18.28	18.31	18.35	17.72	...	17.75
J0002+0733	2745919102257342976	DA	11.85	18.31	17.84	17.76	17.78	17.83	17.87	17.23	17.07	17.06
J0002+0733	2745919106553695616	DAH	12.19	18.52	18.05	17.98	18.01	18.09	18.15	17.59	17.44	17.51
J0002+1610	2772241822943618176	DA	9.817	19.55	18.93	18.71	18.64	18.67	18.72	17.98	17.66	17.54
J0002+6357	431635455820288128	DC	38.07	...	17.64	16.99	16.72	16.65	16.59	15.8	15.58	15.51
J0003+6512	432177373309335424	DC	10.66	...	17.59	17.61	17.73	17.84	17.94

**Figure 2.** Same as Figure 1 but for the SDSS M_g versus $(u - g)$ colour-magnitude diagram. Also shown are cooling sequences for $0.6 M_{\odot}$ CO-core models for DQ stars (cyan) with $\log C/He = -5$ (left) and -7.5 (right), and for DZ stars (yellow) with $\log Ca/He = -11.5$ (left) and -7 (right).

faint luminosities, as well as the inability of pure H models to match the observed faint DC sequence.

3 MODEL ATMOSPHERE ANALYSIS

3.1 The Photometric Technique

The physical parameters of the white dwarfs in our sample can be measured using the so-called photometric technique, described at length in Bergeron et al. (1997). Briefly, the optical and near-infrared photometry are first converted into average fluxes in each bandpass

using the equations given in Holberg & Bergeron (2006) appropriate for magnitudes on the AB system for the SDSS u and Pan-STARRS $grizy$ optical photometry, or on the Vega system for the near-infrared JHK photometry, with zero points calculated for each filter system (2MASS, MKO, VISTA, Bessell, etc.). The synthetic photometry is calculated for each model grid described below, by integrating the monochromatic Eddington fluxes – which depend on T_{eff} , $\log g$, and chemical composition – over each filter bandpass. The observed and model fluxes are related to each other by the solid angle, $\pi(R/D)^2$, where R is the stellar radius and D is the distance from Earth, which can be obtained from the Gaia trigonometric parallax measurements; given that our sample is limited to objects with $> 10\sigma$ significant parallax, it is justified to simply assume here $D = \varpi^{-1}$. A χ^2 value is calculated as the difference between observed and predicted fluxes summed over all bandpasses, and minimized using the nonlinear least-squares method of Levenberg-Marquardt (Press et al. 1986), which is based on a steepest decent method. Only T_{eff} and the solid angle $\pi(R/D)^2$ are considered free parameters for an assumed chemical abundance, while the uncertainties of both parameters are obtained directly from the covariance matrix of the fit. The stellar radius is then converted into mass using the evolutionary models described in Section 2.3. We use thick ($q(\text{H}) = 10^{-4}$) and thin ($q(\text{H}) = 10^{-10}$) H-layer models for H- and He-dominated atmospheres, respectively. Bad photometric data points are excluded from our fits after visual inspection, and displayed in red in the fits presented below.

3.2 DA White Dwarfs

Our model atmospheres for DA white dwarfs are described at length in Tremblay et al. (2011) and references therein, and in Blouin et al. (2018a) for $T_{\text{eff}} < 5000$ K, where additional nonideal effects are taken into account. We assume a pure hydrogen atmospheric composition for the 1764 DA stars in our sample³. This is a perfectly legitimate assumption, as discussed in Bergeron et al. (1997, see also Blouin et al. 2019). A fit to a typical DA star, J0034+1517, is displayed in Figure 3. We also provide the Gaia ID as well as the spectral type. The observed photometry is shown as error bars (1σ uncertainty) while the particular set of photometry used is indicated at the top left of the upper panel. In the case of the near-infrared JHK photometry, we use a lower subscript to specify the particular system used (M: MKO, 2: 2MASS, B: Bessell, V: VISTA). Our best-fit model is represented by solid dots, with the corresponding

³ We exclude the 17 He-rich DAs and the 4 DA + DQ unresolved systems, which are analysed further below.

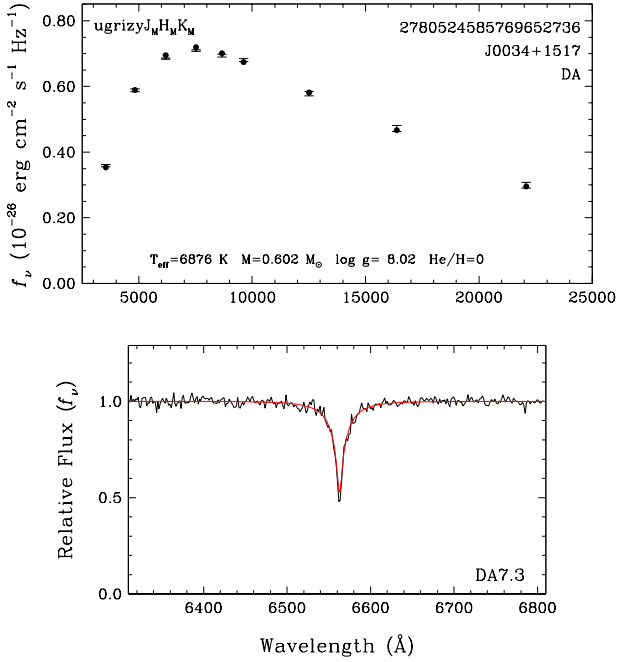


Figure 3. Best fit to a typical DA star in our sample. The observed photometry is shown as error bars (1σ uncertainty in all figures) and the photometric set used is indicated at the top left of the upper panel (see text). Our model atmosphere fit is shown as solid dots, with the parameters given in the upper panel. The lower panel shows the normalized optical spectrum (black), compared with the model spectrum (red) interpolated at the parameters obtained from the photometric solution.

parameters given in the upper panel. The bottom panel shows the optical spectrum, normalized to a continuum set to unity, compared to the model spectrum (in red) interpolated at the parameters obtained from the photometric solution and convolved with the appropriate spectral resolution. Hence, it is not a formal fit, but it is used instead to validate our photometric solution. An observed discrepancy might be indicative of an unresolved double degenerate binary (see Section 3.9), or of an incorrect assumption about the chemical composition (see Section 3.3). Depending on the spectral coverage, we show the region near $H\alpha$, $H\beta$, or even $H\gamma$, in cases where the red part of the spectrum is contaminated by the presence of an M-dwarf companion. We also provide in the lower panel the spectral type with the temperature index defined as $50,400/T_{\text{eff}}$.

Among our sample of DA white dwarfs, we also have 50 DAZ stars, where in the present context we refer to white dwarfs with H-dominated atmospheres and metal lines visible in their optical spectra, in particular the Ca II H & K doublet. If metal lines are detected, which is the case for 34 DAZ stars in our sample, we determine the Ca abundance by fitting the Ca II H & K doublet using a grid of model atmospheres with $T_{\text{eff}} = 4500$ (500) 9000 K and $\log \text{Ca}/\text{H} = -10.5$ (0.5) -5.5 , where the numbers in parentheses indicate the step size. We assume chondritic abundance ratios with respect to Ca for other metals. The same model grid is also used in Section 3.5 to analyse cool H-atmosphere DZ and DZA white dwarfs.

The fits to all white dwarfs in our sample are provided as Supplementary Material. For the fits to DA and DAZ white dwarfs, we display both the pure H and mixed H/He solutions (with H as a trace element, see Section 3.7); the entire spectrum is also shown in a

third panel at the bottom. In some cases there is no optical spectrum available to us, and we simply rely on the published spectral type. In general, the predicted model spectra are in excellent agreement with the observed absorption profiles. Exceptions include of course the magnetic DA white dwarfs (see, e.g., J0505–1722) since all our models are for non-magnetic stars (see also Section 3.8). We note that $H\alpha$ can be detected in DA stars as cool as $T_{\text{eff}} \sim 4800$ K (see J0717+1125), although this depends on the surface gravity of the white dwarf, and most importantly, on the signal-to-noise ratio of the optical spectrum.

3.3 He-rich DA White Dwarfs

Several DA stars in our sample have He-rich atmospheres. The origin of these so-called He-rich DA white dwarfs can be explained in terms of DA stars with thin hydrogen layers that turn into a He-rich white dwarf below $T_{\text{eff}} \sim 12,000$ K as a result of convective mixing. If the object is hot enough, $H\alpha$ might still be detectable as a shallow absorption feature, heavily broadened by van der Waals interactions. Classical He-rich DA white dwarfs include Ross 640, L745-46A, and GD 95, all three of which also show traces of metals (see Figure 14 of Giammichele et al. 2012). Many additional He-rich DA white dwarfs have also been identified and analysed by Rolland et al. (2018). As these stars cool off, the $H\alpha$ absorption feature rapidly falls below the limit of visibility (see Figure 14 of Rolland et al. 2018).

The 17 He-rich DA white dwarfs in our sample have been fitted using mixed H/He model atmospheres similar to those described above for DA stars, but with $\log \text{H}/\text{He} = -5.0, -4.0$ (0.5) -1.0 (1.0) $+2.0$. We use the same photometric method as for DA stars, but this time we explore all values of H/He individually and simply adopt the solution that most closely matches the observed $H\alpha$ profile. A fit to a typical He-rich DA star in our sample, J1024–0023, is displayed in Figure 4. Here we show both the pure H and mixed H/He solutions, as well as the corresponding predicted spectra at $H\alpha$. As can be seen, the observations at $H\alpha$ clearly rule out the pure H solution for this object, whereas the mixed H/He solution constrained by $H\alpha$ provides a much better fit to the observed photometry, in particular in the *ugr* passbands.

We also found in our sample what appears to be normal DA stars – with the complete Balmer series detected – for which we achieve a much better fit in the *ugr* passbands by assuming a mixed composition of $\log \text{H}/\text{He} = -1.0$ (see J1611+1322 and J2138+2309 in the Supplementary Material), although we do not necessarily achieve better fits at $H\alpha$. Also, two He-rich DA stars in our sample (J0103–0522, J1159+0007) show asymmetric Balmer line profiles. Tremblay et al. (2020) suggested that J0103–0522 was magnetic. However, the fact that J0103–0522 and J1159+0007 are almost identical twins, and that they both have He-rich atmospheres, suggests instead that the asymmetric profiles are the result of some unusual line broadening due to helium, unaccounted for in our models, a hypothesis supported by the recent calculations of Spiegelman et al. (2022, see their Figures 7 and 8). Similar asymmetric profiles can also be observed in the spectrum of GD 16 (see Figure 18 of Limoges et al. 2015), another He-rich DA star (a DAZB white dwarf in this case). Clearly, these peculiar white dwarfs deserve further investigation.

3.4 DQ White Dwarfs

We fit the 146 DQ white dwarfs in our sample with spectra available (including the four DA + DQ systems) using a hybrid spectroscopic and photometric method outlined in Dufour et al. (2005), although

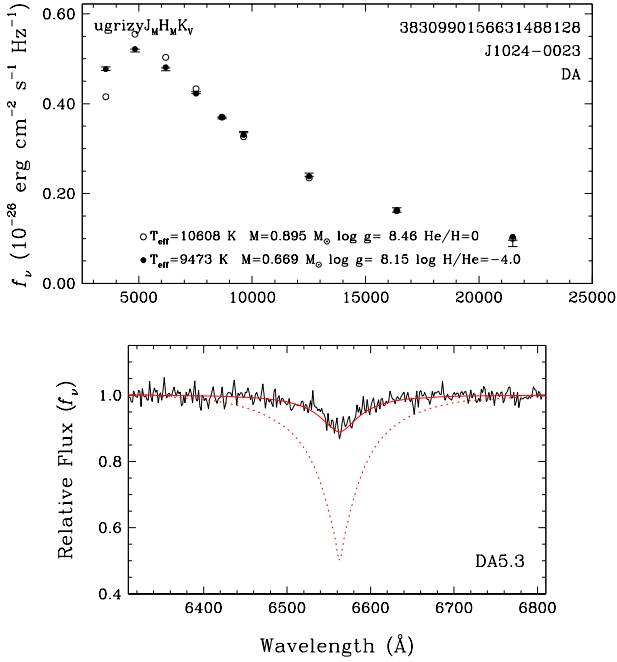


Figure 4. Best fit to a typical He-rich DA star in our sample. The observed photometry is shown as error bars and the photometric set used is indicated at the top left of the upper panel. Our model atmosphere fits for pure hydrogen and mixed H/He compositions are shown with different symbols, with parameters given in the upper panel. The lower panel shows the normalized optical spectrum (black), compared with the model spectra (red) interpolated at the parameters obtained from the photometric solution (solid line: mixed H/He solution, dotted line: pure H solution). Note that the y-axis begins at 0.4.

we rely here on the improved models of [Blouin et al. \(2018a, 2019\)](#), and [Blouin & Dufour \(2019\)](#). We first assume a carbon abundance and fit the photometry using the same technique as before. We then fit the optical spectrum – neutral carbon lines or C₂ Swan bands – to measure the carbon abundance using the T_{eff} and $\log g$ values obtained from the photometric solution. We iterate this procedure until we reach an internal consistency between the photometric and spectroscopic solutions. A fit to a typical DQ star in our sample, J0705–1703, is displayed in Figure 5.

Some DQ stars in our sample also show a weak and broad H α absorption feature (J0916+1011, J0950+3238, and J1147+0747) and are thus genuine DQA white dwarfs. In some cases, however, the presence of hydrogen lines is better explained as the result of an unresolved DA+DQ double degenerate binary (J0613+2050, J0928+2638, J1406+3401, and J1532+1356). In these cases, not only the object appears overluminous, but hydrogen lines are also much sharper, in contrast to the genuine DQA stars where H α is heavily broadened by van der Waals interactions in a He-dominated environment. For the three genuine DQA white dwarfs, we calculated a smaller set of model atmospheres that also include hydrogen with $\log \text{H}/\text{He} = -5, -4, \text{ and } -3$, and constrain the hydrogen abundance to the closest value set by the observations at H α . For the four DA+DQ systems, we did not attempt to deconvolve the individual components, and simply fit these systems assuming a single DQ white dwarf; these are further discussed in Section 3.9.

Given the temperature range explored in our analysis, most DQ stars in our sample show only C₂ Swan bands, although some of

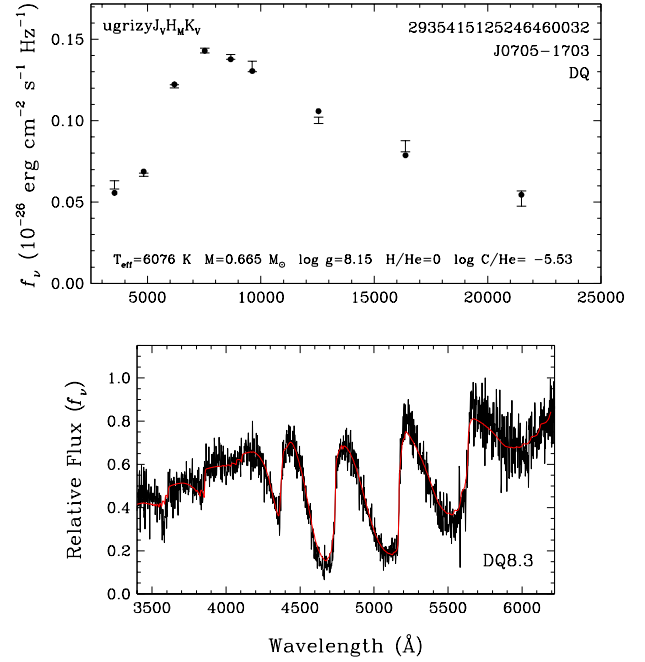


Figure 5. Best fit to a typical DQ white dwarf in our sample. Upper panel: The observed photometry, indicated at the top left, is shown by error bars, while the model atmosphere fit is shown by solid dots, with parameters given at the bottom. Lower panel: Optical spectrum (black) used to constrain the carbon abundance of the photometric solution, compared with the model spectrum (red).

the hottest ones (e.g., J0859+3257) also show neutral carbon lines. In general, the strong shift of the Swan bands, as modeled by [Blouin & Dufour \(2019\)](#) and references therein, is remarkably well reproduced (e.g., J1333+0016), although there are several exceptions and problematic cases (e.g., J1113+0146, J1618+0611), already discussed by [Blouin & Dufour](#) (see their Section 3.1). Possible explanations include problems with the simple model used to account for the distortion of the Swan bands, or the presence of a strong magnetic field, which has been confirmed by spectropolarimetric measurements in some objects.

Finally, we could not help noticing that some of the DQ white dwarfs in our sample appear to show some IR flux deficiency, the best example of which is J1442+4013. Other examples in our sample include J0033+1451, J0041–2221 (the well-studied LHS 1126; [Wickramasinghe et al. 1982](#); [Bergeron et al. 1994](#); [Kilic et al. 2006](#); [Blouin et al. 2019](#)), J0508–1450, J1045–1906, J1247+0646, and J1614+1728. Indeed, our poor photometric fits to these stars are reminiscent of the poor fits we obtain for the so-called IR-faint white dwarfs (see Section 3.6), when analysed with pure H or pure He models instead of mixed H/He models. In these cases, the IR-flux deficiency is the result of collision-induced absorptions (CIA) by molecular hydrogen due to collisions with helium. Perhaps the IR flux deficiency in these peculiar DQ stars is also the result of absorption by molecular hydrogen, thus offering the possibility of measuring H abundances in cool DQ white dwarfs. Unfortunately, our attempts to fit these DQ white dwarfs with mixed H/He/C model atmospheres were unsuccessful, the main problem being that a strong CH absorption feature is always predicted but not observed (with the

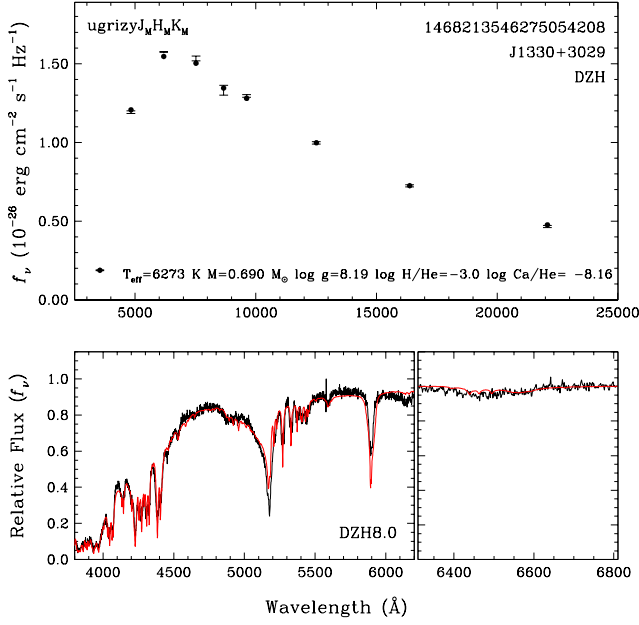


Figure 6. Best fit to a typical DZ white dwarf in our sample. Upper panel: The observed photometry, indicated at the top left, is shown by error bars, while the model atmosphere fit is shown by solid dots, with parameters given at the bottom. Lower panel: Optical spectrum (black) used to constrain the metal abundance (left) and hydrogen abundance (right) of the photometric solution, compared with the model spectra (red).

possible exception of J1442+4013). Clearly, these objects deserve further investigation.

3.5 DZ White Dwarfs

The procedure used to fit the DZ and DZA white dwarfs in our sample is similar to the approach used for DQ stars, with model atmospheres described in Blouin et al. (2018a, see also Coutu et al. 2019). The only exception here is that we also rely on optical spectra around $H\alpha$, if available, to measure (or constrain) the hydrogen abundance. Our solutions are provided in terms of the Ca abundance ($\log \text{Ca}/\text{He}$), and we assume chondritic abundance ratios with respect to Ca for other metals, spectroscopically visible or not. Our model grid covers Ca abundances of $\log \text{Ca}/\text{He} = -12.0$ (0.5) -7.0 . As was the case for the He-rich DA white dwarfs, we do not attempt to fit the hydrogen abundance, but we simply explore the solutions with various hydrogen abundances ($\log \text{H}/\text{He} = -5, -4, -3, -2, -1.5$, and -1) and adopt the value, or limit, consistent with the $H\alpha$ spectrum. A fit to a typical DZ star in our sample, J1330+3029, is displayed in Figure 6. Even though the object shown here shows various metallic absorption features, most DZ stars in our sample only show the Ca II H & K doublet.

We have 9 DZ stars in our sample without optical spectra available to us. For 4 of those, we rely on Ca abundance published in the literature (J0124–2229, J0512–0505, J0823+0546, and J2343–1659), while we fit the remaining 5 (J0153+0911, J0733+2315, J1442+0635, J1551+1439, and J2147–2910) using the procedure for DC stars described in Section 3.7.

An important issue in our analysis is whether the cool DZ and DZA stars in our sample are H- or He-atmosphere white dwarfs (see, e.g., Blouin & Xu 2022). To explore this possibility, we fitted all relevant objects with the He-atmosphere DZ model grid described above, and

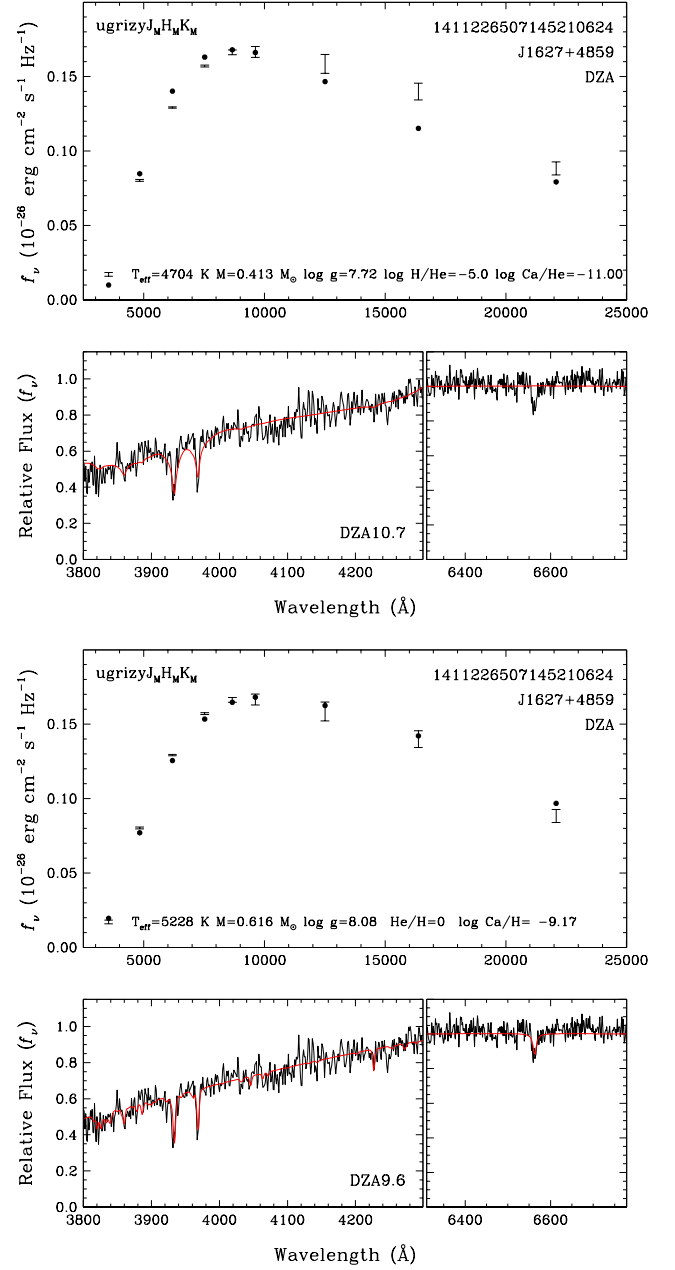


Figure 7. Same as Figure 6 but for a DZA star fitted under the assumption of a He-atmosphere (top two panels) and H-atmosphere (bottom two panels) white dwarf.

compared the solutions with those obtained from the model grid for H-atmosphere DAZ white dwarfs described in Section 3.2. We found out that it was rather easy to discriminate both solutions by simply looking at the quality of the fits. But more importantly, we also found that all cool, low-mass ($M < 0.45 M_{\odot}$) DZ and DZA stars uncovered using He-atmosphere models turned out to be H-atmosphere white dwarfs, with much larger masses. A good example is displayed in Figure 7 for the DZA white dwarf J1627+4859, where we contrast both solutions. Here the mass obtained using H-atmosphere models, $M = 0.616 M_{\odot}$, is significantly larger than that obtained using He-atmosphere models, $M = 0.413 M_{\odot}$. The overall quality of the fit is also far superior using H-atmosphere models.

3.6 IR-faint White Dwarfs

Bergeron et al. (2022) have recently demonstrated that white dwarfs showing a strong infrared flux deficiency resulting from collision-induced absorption (CIA) by molecular hydrogen – often referred to as ultracool white dwarfs – are not so cool after all. Indeed, model atmospheres including the high-density correction to the He^- free-free absorption coefficient of Iglesias et al. (2002) have been shown to yield significantly higher effective temperatures and larger stellar masses than previously reported. Hence, these objects should be more accurately referred to as IR-faint white dwarfs.

We have 47 IR-faint white dwarfs in our sample, 43 of which have been previously analysed in Bergeron et al. (2022). With the exception of J0041–2221 (LHS 1126), which we analyzed above as a DQ white dwarf, we fit the IR-faint white dwarfs in our sample using the same models as those described at length in Bergeron et al. These are all DC white dwarfs with the exception of the four previously known DZ stars J0804+2239, J1824+1212, J1922+0233, and J2317+1830 (Blouin et al. 2018b; Tremblay et al. 2020; Hollands et al. 2021). The four new IR-faint white dwarfs discovered in our analysis are J0223+2055, J0910+2554, J1801+5050, and J2347+0304. Three of these have comparable temperatures ($T_{\text{eff}} \sim 4500$ K) and stellar masses ($M \sim 0.5 M_{\odot}$), but more importantly, comparable chemical compositions in the range $\log \text{H}/\text{He} \sim -1.0$ to 0.1 (i.e., nearly equal amounts of H and He compared to other IR-faint white dwarfs). Our best fit to J1801+5050 is displayed in Figure 8. These four new discoveries had not been identified as IR-faint candidates in Bergeron et al. because their colours in the Pan-STARRS M_g versus $(g-z)$ colour-magnitude diagram put them near the bulk of white dwarfs along the faint end of the main white dwarf sequence, making them impossible to identify without proper near-infrared photometry. We come back to this important point in Section 3.7.1.

3.7 DC White Dwarfs

The procedure used to fit the 810 DC white dwarfs in our sample (excluding the IR-faint DC stars) is identical to the approach used above for the DA stars (including the model atmospheres). A fit to a typical DC star in our sample, J1240+0932, is displayed in Figure 9. So far, it was possible for the previous spectral types to obtain an almost unique solution because the information contained in the optical spectrum (or the *JHK* photometry in the case of IR-faint white dwarfs) allowed us to constrain the chemical composition, whether it is the main constituent, hydrogen or helium, or traces of other elements (hydrogen, carbon, metals).

For genuine DC stars with featureless spectra, it becomes extremely difficult to determine even the main constituent of the atmosphere, unless the object is hot enough that $\text{H}\alpha$ would be detected if the atmosphere were composed of hydrogen. The case of J1240+0932 displayed in Figure 9 is such an example. Moreover, as demonstrated in Bergeron et al. (2019), invisible traces of hydrogen in He-atmosphere DC white dwarfs can affect the temperature and mass determinations significantly when using the photometric technique (see also Figure 5 of Blouin et al. 2019), and the exact amount of hydrogen present is impossible to determine accurately. The only exception is for IR-faint DC white dwarfs where the presence of hydrogen can be inferred, and thus measured, from the strong infrared absorption resulting from collision-induced absorption by molecular hydrogen, whether it is due to $\text{H}_2\text{-H}_2$ or $\text{H}_2\text{-He}$ interactions, but this becomes only possible at low effective temperatures ($T_{\text{eff}} \lesssim 6000$ K) when molecular hydrogen starts to form.

In principle, it is theoretically possible to distinguish H-rich from

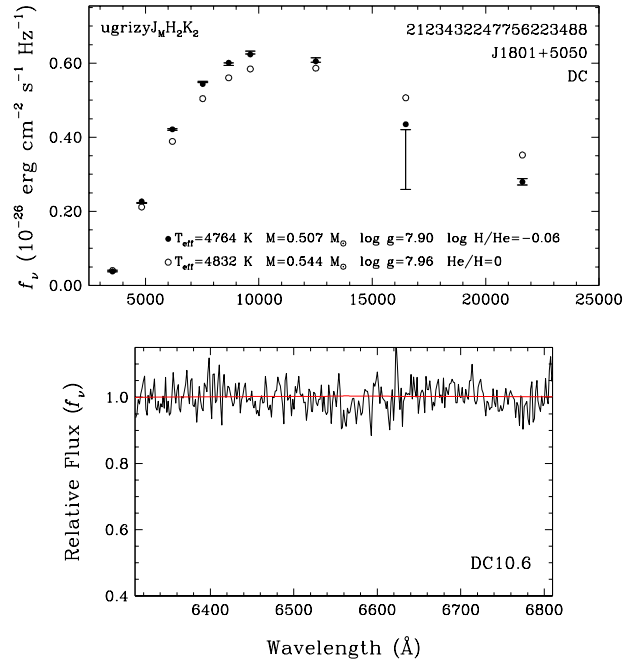


Figure 8. Best fit to a new IR-faint white dwarf identified in our sample. Upper panel: The observed photometry, indicated at the top left, is shown by error bars, while the model atmosphere fit is shown by solid dots for the mixed H/He solution, and open circles for the pure H solution, with parameters given at the bottom. Lower panel: Optical spectrum (black) compared with the model spectrum (red) interpolated at the parameters obtained from the pure H photometric solution.

He-rich white dwarfs over a wide range of effective temperatures due to the different behaviour of H and He continuum opacities, but this requires extremely precise photometry, and more importantly, a very accurate magnitude-to-flux conversion, which is not always the case, even for Pan-STARRS and SDSS magnitudes based on the AB photometric system, as discussed by Bergeron et al. (2019). The problem becomes even more severe when multiple photometric systems are combined, for instance optical and infrared photometry. Consequently, it is extremely dangerous to allow the H/He abundance ratio to be a free parameter for fitting DC white dwarfs, as emphasized in Blouin et al. (2019). We propose a different statistical approach below.

3.7.1 The Bottom of the Cooling Sequence

We first investigate in this section the nature of the cool DC white dwarfs at the faint end of the cooling sequence in the colour-magnitude diagrams displayed in Figures 1 and 2. In both diagrams, the $0.6 M_{\odot}$ CO-core models with pure H (solid lines) and pure He (dotted lines) atmospheres fail to match the faint sequence of DC white dwarfs, although the pure H models are definitely much closer than the pure He models. Even though the mixed $\log \text{H}/\text{He} = -5$ models (dash-dotted lines) match the DC sequence rather well in the SDSS M_g versus $(u-g)$ colour-magnitude diagram, they fail miserably in the Pan-STARRS M_g versus $(g-z)$ diagram due to the onset of CIA. We also notice that there are very few objects observed along the pure He sequence at faint luminosities, suggesting that most cool DC white dwarfs have H-dominated atmospheres, at

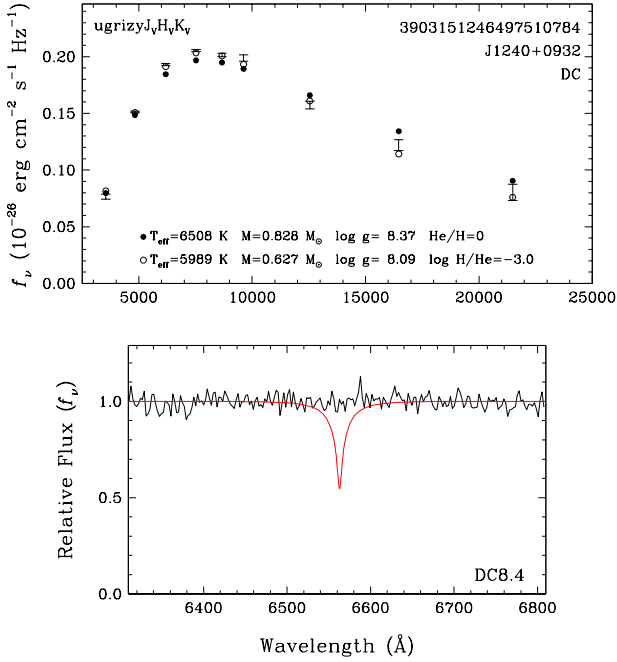


Figure 9. Best fit to a typical DC white dwarf in our sample. Upper panel: The observed photometry, indicated at the top left, is shown by error bars, while the model atmosphere fit is shown by solid dots for the pure H solution, and open circles for the mixed H/He solution, with parameters given at the bottom. Lower panel: Optical spectrum (black) compared with the model spectrum (red) interpolated at the parameters obtained from the pure H photometric solution.

least based on these diagrams. Furthermore, we can see in Figure 1 that the pure hydrogen sequence provides an excellent match to the DA stars at higher temperatures, and that the departure occurs below roughly $T_{\text{eff}} \sim 5300$ K, when $H\alpha$ becomes difficult to detect. But from an empirical point of view, the DA sequence at this temperature merges perfectly well with the cool DC sequence. All these observations strongly suggest a problem with the physics of pure-H model atmospheres at very low effective temperatures.

We investigated this problem by looking at one of the coolest objects along the DC sequence, J1102+4112, with $M_g = 17.28$ and $(g - z) = 2.01$ (the reddest DC star in Figure 1). This object has also been analysed in detail by Hall et al. (2008). Our best photometric fit under the assumption of a pure H atmosphere is displayed in Figure 10. Here we show two fits, one by including the near-infrared *JHK* photometry (the solution shown in black), and the other solution (in red) where the *JHK* photometry has been omitted. Although both fits are far from perfect, they are significantly superior to those obtained with mixed H/He or pure He atmospheres (not shown here), two solutions that can be easily ruled out. Similar conclusions have been reached by Hall et al. (2008, see their Figures 4 and 5). The results shown in Figure 10 also indicate that the solution based solely on optical *ugrizy* photometry yields a low temperature of $T_{\text{eff}} = 3500$ K, and a low mass of $M = 0.465 M_{\odot}$. However, the inclusion of the near-infrared *JHK* photometry has the effect of pushing the solution towards a higher temperature of $T_{\text{eff}} = 3800$ K, and a much larger

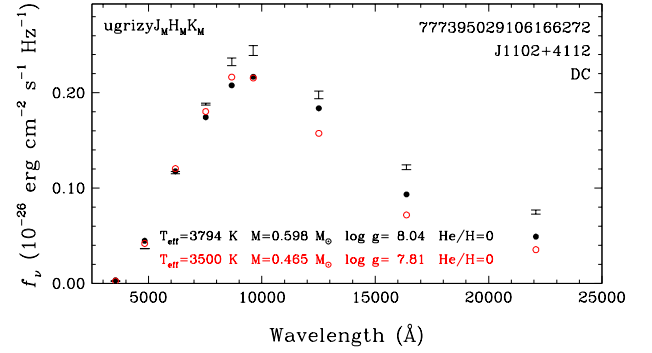


Figure 10. Best fits to one of the coolest DC white dwarfs in our sample assuming a pure H composition. The observed photometry, indicated at the top left, is shown by error bars. The filled black dots show the fit obtained by including the near-infrared *JHK* photometry, while the open red dots show the solution obtained by fitting only the optical *ugrizy* photometry. The corresponding parameters are given at the bottom.

mass of $M = 0.598 M_{\odot}$ – i.e., $\sim 0.13 M_{\odot}$ larger – in much better agreement with the average mass of white dwarfs.⁴

We observe a similar effect in all cool DC white dwarfs in our sample, but to a lesser extent as we go up in temperature. And again, the pure He model atmospheres yield far worse solutions, in particular in terms of mass. This can be appreciated by examining the mass versus effective temperature distribution for all the cool ($T_{\text{eff}} \lesssim 5500$ K) DC white dwarfs in our sample, displayed in Figure 11, obtained under the assumption of pure H (red symbols) and pure He (blue symbols) atmospheric compositions. Note that for the objects below $0.2 M_{\odot}$, we rely on the He-core models described in Bergeron et al. (2022, see their Figure 3), which are appropriate in the temperature range considered here. We can see that the T_{eff} and M values obtained under the assumption of pure He compositions are unrealistically low. This result is entirely consistent with the prediction of the $0.6 M_{\odot}$, pure He sequence in the colour-magnitude diagram displayed in Figure 1 with respect to the location of these cool DC stars; the models need to be more luminous, thus requiring larger radii and smaller masses. In contrast, the masses obtained under the assumption of pure H models in Figure 11 are much closer to the mean mass of white dwarfs, although we see a definite trend towards lower masses at lower temperatures, another indication of problems with the physics of pure H model atmospheres at low effective temperatures, and thus higher photospheric densities, a conclusion also reached by Hall et al. (2008).

We can now understand more quantitatively the results displayed in Figure 12 of Bergeron et al. (2019), which shows similar M versus T_{eff} distributions for all white dwarfs found in Gaia within a distance of 100 pc, including both spectroscopically identified white dwarfs as well as white dwarf candidates. In this case, the stellar parameters have been determined using photometric fits to Pan-STARRS *grizy* photometry only. Their solutions obtained from pure H (top panel) and pure He (middle panel) model atmospheres show the same behavior as in Figure 11, with the exception that our masses based on

⁴ Note that Leggett et al. (2018) erroneously obtained a mixed H/He solution for this object (WD 1059+415 in their Table 4), although they also show (see the supplementary material) their best fit assuming a pure H composition, which is almost identical to that shown here. Their pure H solution fit even provides an excellent match to the Spitzer photometry.

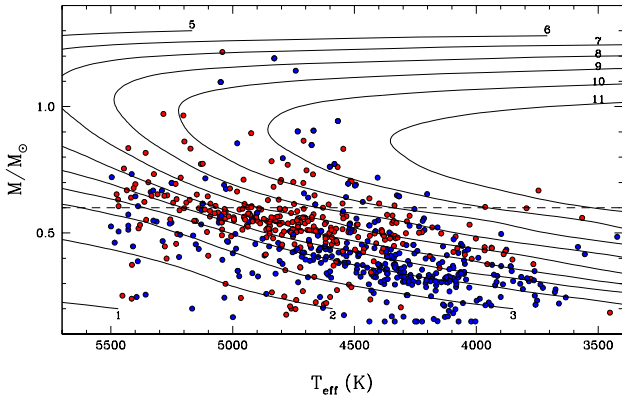


Figure 11. Mass as a function of effective temperature for the cool DC white dwarfs in our sample under the assumption of pure H (red dots) and pure He (blue dots) atmospheric compositions. The dashed line corresponds to $0.6 M_{\odot}$, the average mass for white dwarfs. Solid curves are theoretical isochrones (white dwarf cooling age only), labeled in units of 10^9 yr, obtained from the CO-core cooling sequences described in Section 2.3 with thick H layers ($q(\text{H}) = 10^{-4}$).

pure H models are larger due to the use of *JHK* photometry for many of our objects, but still not enough to reach the $\sim 0.6 M_{\odot}$ average mass for white dwarfs for the coolest DC stars in our sample.

All the results above strongly support the idea, also suggested by Kowalski & Saumon (2006), that the bulk of cool ($T_{\text{eff}} \lesssim 5000$ K) DC white dwarfs, but not all (see below), probably have H atmospheres. By taking into account the suspected problems with the H-atmosphere models, we did not find a single convincing case of a cool, pure He DC white dwarf in our sample. Note that we exclude from the discussion the cool DZ white dwarfs, which are discussed further below. The fact that the $0.6 M_{\odot}$ pure H theoretical sequence in Figure 1 does not match the observed DC sequence is obviously related to the less-than-perfect fit displayed in Figure 10, in particular in the optical.

One possible explanation for this problem is the UV/blue opacity originating from the red wing of $\text{Ly}\alpha$. Kowalski & Saumon (2006) performed such calculations and successfully demonstrated that models including this opacity show significant improvements in explaining the location of DC white dwarfs in colour-colour diagrams (see their Figure 4). Note that their calculations are based on the one-perturber approximation, H or H_2 , and it is possible that the interaction from multiple perturbers (see, e.g., Allard & Kielkopf 2009) need to be taken account in the coolest white dwarfs where the densities are significantly larger. We also note that Saumon et al. (2014) analysed Hubble Space Telescope STIS spectra of eight very cool WDs (five DA and three DC stars) and showed that their fits become worse at lower T_{eff} and higher $\log g$ values. As the authors conclude, these are the stars with higher photospheric densities and more extreme physical conditions, implying that the microphysics of dense matter probably needs to be revised.

It is also possible that other sources of opacity might be responsible for the problems described above. For instance, the top panel of Figure 17 from Saumon et al. (2022) shows that at the photosphere of a pure H model at $T_{\text{eff}} = 4000$ K, the opacity from the red wing of $\text{Ly}\alpha$ dominates in the UV, while the H^- bound-free opacity and the H_2 - H_2 (and H_2 -H) CIA opacity dominate in the optical and near-

infrared, respectively. Perhaps the physics from these last two opacity sources needs to be revised as well.

As discussed above, the end of the cooling sequence in Figure 1 is composed mainly of DC stars that are better interpreted as H-atmosphere white dwarfs, but not all. The glaring exceptions are the IR-faint DC white dwarfs with mixed H/He compositions. We reproduce in Figure 12 the M_g versus $(g - z)$ colour-magnitude diagram from Bergeron et al. (2022) together with the 105 IR-faint white dwarfs they analysed (in red) as well as the four new objects (in yellow) identified in our survey and discussed in Section 3.6. Most IR-faint white dwarfs in this diagram are located on the nearly horizontal branch, consistent with mixed H/He atmospheres with $\log \text{H/He} \sim -2$, a result confirmed quantitatively by a more rigorous model atmosphere analysis (see Figure 15 of Bergeron et al. 2022). However, these appear more common because they clearly stand out in such a colour-magnitude diagram, an obvious selection effect. But there are other IR-faint white dwarfs more difficult to detect, such as those found on the main branch at the end of the cooling sequence. These include three of the four we identified in our analysis, thanks to the available *JHK* photometry, otherwise they would have gone unnoticed⁵. Note that the parameters determined for three of the new IR-faint white dwarfs identified in our survey ($M \sim 0.5 M_{\odot}$, $\text{H/He} \sim 1$) are entirely consistent with their location in the colour-magnitude diagram, as illustrated in Figure 12, where we overplotted the corresponding cooling sequence (in green). It is therefore possible that many more are hiding in the same region of the colour-magnitude diagram. This stresses the importance of eventually securing *JHK* photometry for all spectroscopically confirmed white dwarfs at the end of the cooling sequence.

3.7.2 The Atmospheric Composition of DC White Dwarfs

As discussed above, it is possible to obtain a unique solution for the physical parameters of cool white dwarfs – effective temperature, stellar mass, atmospheric composition – using the photometric approach given that we have sufficient spectroscopic information (hydrogen, carbon, and metallic absorption features). Even in the case of IR-faint white dwarfs, the H/He abundance ratio can be determined from the CIA opacity in the near and far infrared. However, for most genuine featureless DC white dwarfs, the situation is nearly hopeless. Indeed, as discussed in Bergeron et al. (1997), there are also subtle differences between pure H and pure He spectral energy distributions due to the presence (or absence) of the H^- opacity in the infrared (see their Figure 15), or to the onset of CIA absorption at low temperatures (see, e.g., Figure 1 of Blouin et al. 2019), but such measurements can be extremely difficult and dangerous, in particular given the precision and accuracy (or even availability) of infrared photometric measurements. We adopt here a different approach for the DC white dwarfs in our sample.

Above some T_{eff} value, it is almost impossible to distinguish pure He models from models including a trace of hydrogen. Yet, as shown by Bergeron et al. (2019), even undetectable traces of hydrogen can affect the temperature and mass determinations significantly at all temperatures of interest in our analysis. As a conservative estimate, we adopt $T_{\text{eff}} = 6500$ K as the temperature above which all DC stars are assumed to have mixed H/He compositions. We adopt the same approach as in Kilic et al. (2020, see their Section 3.5) and adjust

⁵ These four IR-faint white dwarfs had not even been identified as potential candidates in the search for additional IR-faint candidates discussed in Section 5.4 of Bergeron et al. (2022)

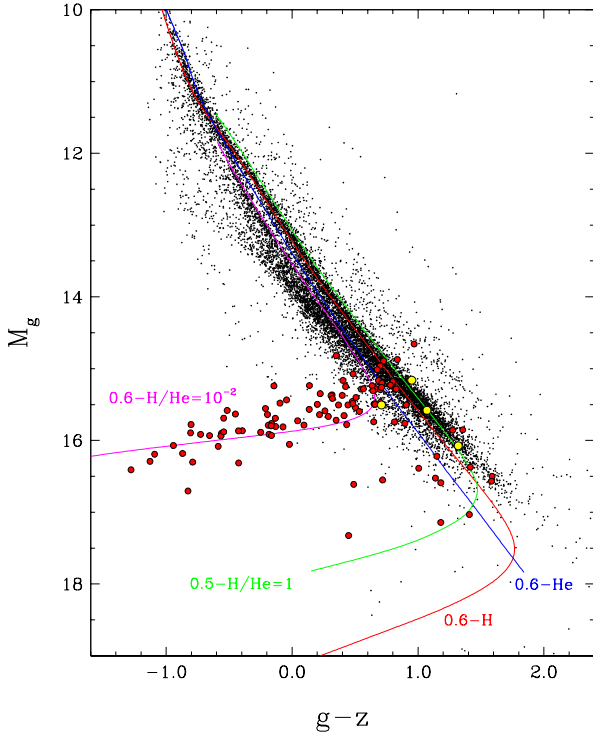


Figure 12. Pan-STARRS M_g versus $(g - z)$ colour-magnitude diagram for the 100 pc sample drawn from the MWDD. The red dots represent the IR-faint white dwarfs analysed in Bergeron et al. (2022), while the yellow dots show the location of the four new objects identified in our analysis. Also overplotted are cooling sequences for $0.6 M_{\odot}$ C/O-core models with pure H (red), pure He (blue), and $\log H/He = -2$ (magenta) atmospheric compositions. The green sequence is for $0.5 M_{\odot}$ C/O-core models with $\log H/He = 0$ (i.e., $H/He = 1$).

the H/He abundance ratio as a function of T_{eff} , from $\log H/He = -5$ at $T_{\text{eff}} = 11,000$ K, up to $\log H/He = -3$ at $T_{\text{eff}} = 6000$ K, thus following the predictions of the convective mixing scenario of Rolland et al. (2018). However, we also found out that assuming $\log H/He = -5$ throughout has little effect on the results (see below). It is of course possible that some of these DC white dwarfs may contain no hydrogen whatsoever, and thus their masses are probably underestimated here, but there is no possible way to identify those in our sample, neither spectroscopically, nor photometrically.

As discussed in the previous section, there is empirical evidence that most, but probably not all, extremely cool DC white dwarfs have pure H compositions. Here we adopt $T_{\text{eff}} = 5200$ K as the temperature below which we assume a pure H atmospheric composition for the DC white dwarfs in our sample. This corresponds also roughly to the temperature above which it is possible to distinguish DA and DC stars from the detection of $H\alpha$. It is of course possible to detect theoretically $H\alpha$ at much lower temperatures, a value that also depends on $\log g$, but the spectral classification is particularly sensitive to the signal-to-noise ratio of the observations. For instance, we can detect a weak $H\alpha$ feature in the DA star J0700+3157 at $T_{\text{eff}} \sim 4900$ K, but this is an extremely high S/N spectrum obtained with the Hale 5 m reflector at Palomar Observatory by Greenstein (1986), who contributed to reclassify many DC white dwarf as DA stars. Similar results have been reported by Bergeron et al. (1997, 2001).

Finally, there is a particular range in temperature between roughly

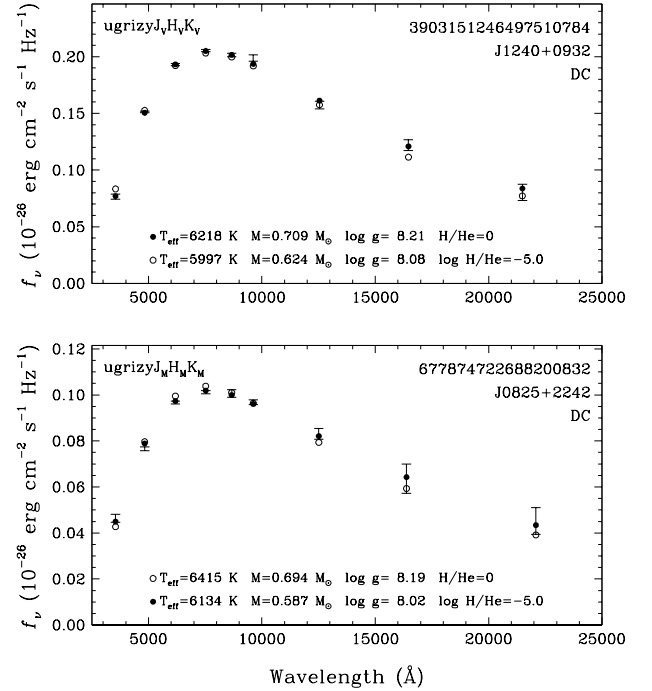


Figure 13. Two DC stars in our sample that are better fit with pure He (top) or mixed H/He (bottom) model atmospheres. The observed photometry is shown as error bars and the photometric set used is indicated at the top left of each panel. Our best model fit, pure He or mixed H/He ($\log H/He = -5$), is shown as solid dots, while the other solution is shown as open circles with the model parameters given in each panel.

$T_{\text{eff}} = 5200$ K and 6500 K where the absence of $H\alpha$ clearly rules out a pure H composition, but where the spectral energy distribution remains particularly sensitive to the presence of even small traces of hydrogen due to the onset of the H_2 CIA opacity. We determined that in this range of temperature, it is thus possible to differentiate pure H from He-rich white dwarfs by the presence of $H\alpha$, and to differentiate pure He from mixed H/He atmospheres by inspecting the spectral energy distribution. For instance, we compare in Figure 13 our best fits to two cool DC stars in this temperature range, obtained with pure He and mixed H/He ($\log H/He = -5$) compositions. J1240+0932 (top) is an example of a DC star that is better fit under the assumption of a pure He atmosphere, while J0825+2242 (bottom) is better fit by a mixed H/He atmosphere, a conclusion that can be drawn by a simple inspection of the fits, but also confirmed from our χ^2 analysis. Note that the small trace of hydrogen of only $\log H/He = -5$, which is much smaller than the hydrogen abundances inferred in IR-faint white dwarfs (see Figure 15 of Bergeron et al. 2022), can affect both the temperature and mass determinations significantly. Moreover, a comparison of the $\log H/He = -5$ solution for J1240+0932, displayed here, with the $\log H/He = -3$ solution previously shown in Figure 9 for the same object, indicates that the particular H/He value used for DC stars in this temperature range (and above) does not affect the parameter determinations significantly.

To summarize, for temperatures between $T_{\text{eff}} = 5200$ K and 6500 K, we adopt the pure H solution for DA stars, while for DC stars we adopt the pure He or mixed H/He solution based on a simple χ^2 analysis. We stress that this approach remains approximate because not all white dwarfs have near-infrared photometry available,

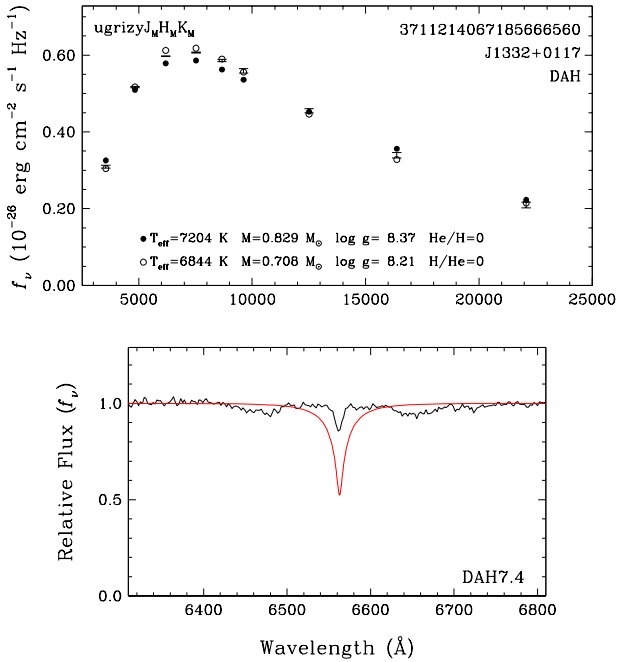


Figure 14. Best fit to a magnetic DA star in our sample. The observed photometry is shown as error bars and the photometric set used is indicated at the top left of the upper panel. Our pure H and pure He model atmosphere fits are shown as solid and open circles, respectively, with the parameters given in the upper panel. The lower panel shows the normalized optical spectrum, compared with the model spectrum (in red) interpolated at the parameters obtained from the pure H photometric solution.

and even for those that do, the quality of the photometry is highly variable.

3.8 Magnetic White Dwarfs

We have several magnetic white dwarfs in our sample of various spectral types. Among those, the more obvious are the magnetic DA stars, with Zeeman splitting in the form of a triplet at $H\alpha$ for a moderate field (see, e.g., Figure 14), or with more displaced and distorted components if the magnetic field is much stronger. We also have several magnetic DQ white dwarfs, although in this case, these are restricted to the very cool DQ stars with strong and shifted C_2 Swan bands (see, e.g., J1038–2040 \equiv LP 790–29). We also have many cases of magnetic DZ stars (see, e.g., J1515+8230). In our analysis, we neglect the existence of these magnetic fields and apply the photometric method using non-magnetic model atmospheres. One obvious effect of using magnetic models is to change the predicted photometry due to absorption lines that are shifted to different wavelengths as a result of the magnetic field. However, we also found cases where even when line blanketing is unimportant, the continuum opacity seems to be affected, an example of which is displayed Figure 14, where we see that the energy distribution is better reproduced by a pure He model rather than a pure H model. We also observe a similar phenomenon in hotter magnetic DA stars, where the Balmer jump appears to be suppressed, in particular in objects with SDSS u magnitudes available (see, e.g., J1126+0906). Despite the better agreement with pure He (or He-rich) models for these stars, we still adopt the pure H solutions for all magnetic DA white dwarfs in our sample.

3.9 Unresolved Double Degenerate Binaries

The existence of unresolved double degenerate binaries (DD) in our sample can already be inferred from the colour-magnitude diagram displayed in Figure 1 where they appear as overluminous objects above the main white dwarf sequence. Indeed, two unresolved white dwarfs of equal luminosity would appear ~ 0.75 mag brighter than a single object, consistent with the location of most overluminous objects in Figure 1 (for systems composed of two $\sim 0.6 M_\odot$ white dwarfs). We also note that most spectroscopically identified overluminous white dwarfs in Figure 1 are DA and DC stars, although we see a few DQ stars as well.

When applying the photometric technique to these DD systems assuming a single star, the radius measurement is usually overestimated since two objects contribute to the total luminosity, and the stellar mass is consequently underestimated as well. However, this may not necessarily be the case if one white dwarf component completely dominates the overall luminosity of the system, in which case the radius and mass measurements remain accurate. If an optical spectrum is available, the spectroscopic technique can be combined with the photometric method to deconvolve the stellar parameters of each component of the system, as done for instance by Bédard et al. (2017, see their Figures 14 to 16).

In our spectro-photometric analysis, we are able to detect the presence of DD systems in various ways. The first is of course when the stellar mass is very low ($M \lesssim 0.48 M_\odot$), because such low-mass white dwarfs cannot have formed within the lifetime of our Galaxy, and can therefore only exist as a result of common envelope evolution. One example in our sample is the DA J0129+1022 with $M = 0.340 M_\odot$. In this particular case, the predicted spectrum at $H\alpha$ is in perfect agreement with the measured parameters obtained from the fit to the energy distribution assuming a single star. Hence, it is possible here that the luminosity of the brighter component of the system completely dominates that of the second component. Alternatively, if two DA components have similar parameters and contribute equally to the total luminosity of the system, we would also reach a perfect agreement between the photometric and spectroscopic solutions. It is of course impossible to distinguish between these two possibilities without a more refined analysis.

In most cases, however, it is expected that the individual components of DA + DA unresolved systems will have different stellar parameters, in which case we may observe a disagreement between the observed $H\alpha$ profile and that predicted from the photometric solution assuming a single star. For instance, J0532+0624 ($M = 0.253 M_\odot$) shows a distorted energy distribution that resembles a He-rich white dwarf, and moreover, the predicted $H\alpha$ profile is at odds with the observations. Another example is J0138–0459 (L870–2, EG 11, WD 0135–052), a classical case of a DD system composed of two DA white dwarfs where both components contribute to the total luminosity of the system, but with significantly different parameters (Bergeron et al. 1989).

Even though all low mass white dwarfs must have formed through binary evolution, the reverse is not necessarily true, and there may exist more normal mass, or even massive, white dwarfs in our sample that are hidden in DD systems. For instance, J0611+0544 ($M = 0.594 M_\odot$), J0904+1349 ($M = 0.611 M_\odot$), and J0929–1732 ($M = 0.632 M_\odot$) are good examples of normal mass white dwarfs with observed inconsistencies in their fits, while J0855–2637 ($M = 0.840 M_\odot$) is a good example of a massive object.

It is also easy to detect the presence of DD systems when the spectral types of both components differ. A good example is J0110+2758 ($M = 0.301 M_\odot$) where the broad and shallow $H\alpha$ feature suggests

the presence of a DC component in the system that dilutes the $H\alpha$ absorption profile. Similarly, we have 11 DQ stars with inferred masses below $0.4 M_{\odot}$ (8 with $M < 0.3 M_{\odot}$), although 4 of these are DD systems composed of a DQ and a cool DA white dwarf (J0613+2050, J0928+2638, J1406+3401, and J1532+1356). Perhaps the remaining 7 objects are also DD systems with the other component being a featureless DC white dwarf. Interestingly, we find no low-mass ($M < 0.4 M_{\odot}$) DZ star in our sample; the only one is the IR-faint white dwarf J1824+1212 ($T_{\text{eff}} \sim 4700$ K).

In what follows, we make no attempt to deconvolve the individual components of DD systems and simply assume that they are single white dwarfs. We just have to keep this in mind when interpreting the physical parameters obtained from our fits.

3.10 White Dwarfs + Companions

Because of the colour cut in the selection of our white dwarf sample, we avoid most WD + M-dwarf binaries, but these systems still exist in our sample, in particular if the M-dwarf has a late type that contaminates the colours, mostly in the near-infrared. In such cases, the M-dwarf companion may contribute significantly to the total flux, which leads to an overestimation of the white dwarf radius, and to an underestimation of its mass. Here we simply exclude the contaminated bandpasses from our photometric fits (these excluded bandpasses are shown in red in our figures). A good example is the DZ white dwarf J1651+6635. Contamination may also occur from different spectral types such as brown dwarfs, like in the case of the DA + L5 system J0135+1445 (NLTT 5306B, Casewell et al. 2020).

3.11 Adopted Parameters

The physical parameters for all white dwarfs in our sample are presented in Table 2, where for each object we provide the J name, Gaia ID (DR2; if not available the EDR3 is given and marked by a star symbol in Table 2), spectral type, effective temperature (T_{eff}), mass (M/M_{\odot}), surface gravity ($\log g$), chemical composition (see below), luminosity ($\log L/L_{\odot}$), and white dwarf cooling age (τ in Gyr).

For clarity, we briefly summarize the procedure used to measure these parameters, and in particular the chemical composition. For DA stars, we assume a pure hydrogen composition ($\text{He}/\text{H} = 0$), with the exception of He-rich DA stars for which the H/He ratio ($\log \text{H}/\text{He}$) is adjusted to match the $H\alpha$ absorption profile. For DQ stars, we provide the carbon abundance ($\log \text{C}/\text{He}$) measured using the optical spectrum. For DZ stars – including DZA and DAZ stars as well –, we give the calcium abundance relative to helium ($\log \text{Ca}/\text{He}$) or hydrogen ($\log \text{Ca}/\text{H}$) depending on the main atmospheric constituent, measured using the metallic features observed in the optical spectrum (all other metals have chondritic abundance ratios with respect to Ca). For IR-faint white dwarfs, we provide the H/He ratio ($\log \text{H}/\text{He}$) obtained from fits to the energy distribution. Finally, for DC stars, we assume a pure hydrogen composition ($\text{He}/\text{H} = 0$) for objects below $T_{\text{eff}} = 5200$ K; between $T_{\text{eff}} = 5200$ K and 6500 K, we adopt the pure He ($\text{H}/\text{He} = 0$) or mixed H/He solution ($\log \text{H}/\text{He}$) based on a χ^2 analysis; for $T_{\text{eff}} > 6500$ K, we also adopt a mixed H/He solution where the hydrogen abundance is adjusted as a function of T_{eff} (as discussed above, the precise hydrogen abundance has little effect on the measured parameters).

4 SELECTED RESULTS

We can now explore the global properties of our sample, which is composed of all white dwarfs identified spectroscopically in the MWDD and with effective temperatures below $T_{\text{eff}} \sim 10,000$ K. As such, it is by no means statistically complete in any sense, although we can expect with such a large sample that all spectral types are statistically well sampled at a given temperature, but probably not as a whole. For instance, Kilic et al. (2020) increased significantly the number of spectroscopically confirmed white dwarfs within 100 pc in the SDSS footprint, but their sample was concentrated above ~ 6000 K where DA stars could be easily identified. Hence, important selection effects are present in our sample, and we make no attempt in our analysis to restrict the results to any particular volume-limited sample.

4.1 Mass Distributions

The mass distribution, M versus T_{eff} , for all 2880 spectroscopically confirmed white dwarfs in our sample are displayed in Figure 15, where the various spectral types are indicated with different colours. Also superposed are theoretical isochrones (WD cooling age only) obtained from cooling sequences with C/O-core compositions, $q(\text{He}) = 10^{-2}$ and $q(\text{H}) = 10^{-4}$; the other curves are described below. In terms of the overall analysis and model atmospheres, this figure is very similar to that shown in Figure 18 of Kilic et al. (2020), with the exception that our analysis is not restricted to the SDSS footprint, it makes use of extensive sets of near-infrared *JHK* photometry, and more importantly, it is not restricted in temperature at the cool end of the white dwarf sequence (Kilic et al. restricted their analysis to $T_{\text{eff}} \geq 6000$ K). There are many interesting features observed in Figure 15, which we now discuss in turn.

We first focus on the region above $T_{\text{eff}} \sim 6000$ K where we can see a nice clustering of objects around the mean mass for white dwarfs ($M \sim 0.6 M_{\odot}$) composed mostly of DA stars, but also a significant fraction of non-DA stars including DC, DZ, and He-rich DA white dwarfs. Note that the normal masses obtained here for the DC stars can only be achieved with model atmospheres containing traces of hydrogen ($\log \text{H}/\text{He} \sim -5$). The same conclusion applies to DZ white dwarfs, but in this case metals are the main source of free electrons. The DQ stars in the same temperature region also form a tight sequence, but with a mean mass $\sim 0.05 M_{\odot}$ lower than average, consistent with the results obtained by Coutu et al. (2019, see their Figure 13). There are at least two possible explanations for this lower mean mass, one involving problems with the physics of DQ model atmospheres (Coutu et al. 2019), and another one recently proposed by Bédard et al. (2022b), who suggested that carbon (and hence the DQ phenomenon) is preferentially detected in lower mass white dwarfs.

There are also two other regions where DA stars are concentrated. The first one is along the crystallization sequence at high mass. To illustrate this process, we indicated by the lower solid blue curve in Figure 15 the region where crystallization starts at the centre of the white dwarf, and by the upper solid blue curve the limit of 80% crystallization of the core resulting from the solidification front moving upward in the star with further cooling. When crystallization occurs, the release of latent heat and chemical fractionation decrease the cooling rate of a white dwarf, leading to this obvious pile up of objects in the M versus T_{eff} diagram observed in Figure 15. Note that the hot end of the crystallization sequence also contains several massive DQ, DC, and He-rich DA white dwarfs. Furthermore, we can clearly see the crystallization sequence merging with the normal-

Table 2. Physical Parameters of the 100 pc White Dwarf Sample. This table is available in its entirety in machine-readable form.

Name	Gaia ID (DR2/EDR3*)	Sp Type	T_{eff} (K)	M/M_{\odot}	$\log g$	Comp	Metals	$\log L/L_{\odot}$	τ (Gyr)
J0000+0132	2738626591386423424	DA	10342 (32)	0.622 (0.007)	8.034 (0.008)	He/H=0	...	-2.79	0.61
J0000+1906	2774195552027050880	DC	5069 (54)	0.553 (0.055)	7.955 (0.066)	He/H=0	...	-4.00	4.86
J0001+3237	2874216647336589568	DC	5753 (56)	0.560 (0.034)	7.981 (0.041)	H/He=0	...	-3.80	3.06
J0001+3559	2877080497170502144	DC	6177 (73)	0.688 (0.031)	8.184 (0.035)	H/He=0	...	-3.79	3.49
J0001-1111	2422442334689173376	DC	6541 (48)	0.651 (0.024)	8.124 (0.027)	$\log \text{H/He} = -3.2$...	-3.65	2.41
J0002+0733	2745919102257342976	DA	7727 (44)	0.598 (0.015)	8.007 (0.018)	He/H=0	...	-3.29	1.23
J0002+0733	2745919106553695616	DAH	8130 (71)	0.805 (0.017)	8.331 (0.02)	He/H=0	...	-3.39	1.90
J0002+1610	2772241822943618176	DA	6684 (42)	0.613 (0.028)	8.037 (0.033)	He/H=0	...	-3.56	1.87
J0002+6357	431635455820288128	DC	4959 (23)	0.596 (0.01)	8.026 (0.011)	He/H=0	...	-4.08	6.55
J0003+6512	432177373309335424	DC	8595 (95)	0.506 (0.014)	7.874 (0.018)	$\log \text{H/He} = -4.0$...	-3.04	0.82

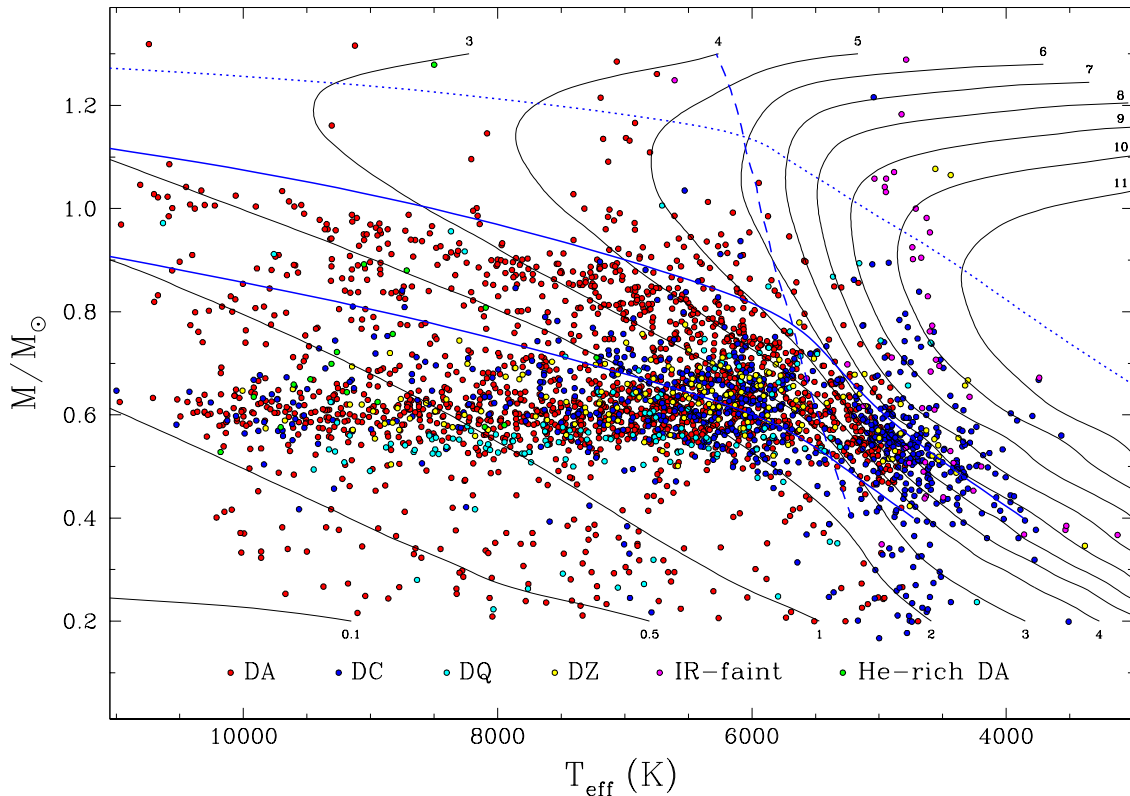


Figure 15. Mass distribution as a function of effective temperature for all 2880 spectroscopically confirmed white dwarfs in our sample for the various spectral types indicated in the legend. Solid black curves are theoretical isochrones (WD cooling age) labeled in units of Gyr, obtained from cooling sequences with C/O-cores, $q(\text{He}) = 10^{-2}$ and $q(\text{H}) = 10^{-4}$ (see Section 2.3). The lower blue solid curve indicates the onset of crystallization at the centre of evolving models, and the upper one indicates the locations where 80% of the total mass has solidified. The dashed curve indicates the onset of convective coupling, while the dotted curve corresponds to the transition between the classical to the quantum regime in the ionic plasma (see text).

mass white dwarf sequence near $T_{\text{eff}} \sim 5500$ K. Incidentally, this also coincides with the temperature where convective coupling occurs at $M \sim 0.6 M_{\odot}$, that is, when the convection zone first reaches into the degenerate interior where all of the thermal energy of the star resides. This is illustrated by the dashed curve in Figure 15, which marks the effective temperature of the onset of convective coupling as a function of mass.

DA stars are also found in large numbers at very low masses ($M \lesssim 0.45 M_{\odot}$). These are most likely unresolved DD binaries, and the low masses inferred here are simply the result of these objects

being overluminous, as observed in Figure 1. For instance, we can calculate that two identical $0.6 M_{\odot}$ unresolved DA white dwarfs would result in a $\sim 0.32 M_{\odot}$ single object in this M versus T_{eff} diagram. But as discussed above, it is also possible that some of these low mass determinations are real if one component of the DD system completely dominates the overall luminosity. Not all low-mass white dwarfs are DA stars, however, and we can see several DQ and DC white dwarfs as well. Not surprisingly, the four DA + DQ unresolved binaries in our sample are found at such low masses. Actually, all four systems have inferred masses well below $0.3 M_{\odot}$ (the DQ stars

J0941+0901, J1135+5724, J1501+2100, and J1803+2320 also have masses below $0.3 M_{\odot}$; if we assume that both the DA and DQ stars in these systems contribute equally to the luminosity, we can calculate the mass of the DQ components to be around $0.52 M_{\odot}$, in excellent agreement with the bulk of single DQ white dwarfs in this temperature range. It is therefore possible that the remaining low-mass DQ white dwarfs in our sample are also DD systems composed of a DQ white dwarf and a featureless DC component. We come back to this point further below. Similarly, it is also possible that the low-mass DC white dwarfs above 6600 K are unresolved binaries, but composed of two normal-mass DC stars, a result that would be consistent with the absence of low-mass DB white dwarfs found in the spectroscopic analysis of Genest-Beaulieu & Bergeron (2019b).

We now turn our attention to the region below $T_{\text{eff}} \sim 6000$ K, where the interpretation of our results becomes significantly more complicated. The most obvious feature in this temperature range is the trend of DA and DC white dwarfs towards lower masses, reaching $M \sim 0.4 M_{\odot}$ at the end of the cooling sequence. We remind the reader that we assumed pure H atmospheres for these DC stars. Had we used pure He or mixed H/He compositions, the situation would have been even worse (see Figure 11). We suggested that improved model atmospheres – most likely related to some inaccurate opacity source – could yield larger masses and higher effective temperatures for these cool DC white dwarfs, and cool DA stars as well, thus filling the apparent gap in the white dwarf distribution observed around $T_{\text{eff}} \sim 5300$ K. Interestingly enough, we can also see that in the same temperature range, several DZ stars appear to follow the $\sim 0.6 M_{\odot}$ sequence nicely, in contrast with the cool DA and DC white dwarfs. In such cool DZ stars, the presence of metals reduces the atmospheric pressure significantly, and thus the effect of collision-induced absorption by molecular hydrogen, if present. In fact, we found that traces of hydrogen have little effect on the measured stellar parameters in this temperature range. Also, we originally identified several low-mass DZ white dwarfs in this temperature range, but it turns out these were H-dominated rather than He-dominated DZ white dwarfs, as discussed in Section 3.5. Given these results, we also explored the possibility that the coolest DC stars in our sample have He-dominated atmospheres containing invisible traces of metals that could affect their temperature and mass determinations. However, the amount of metals required to affect the stellar parameters are large enough that the star would appear as a DZ white dwarf instead of a DC star, a conclusion previously reached by Blouin et al. (2018b). The fact that DZ white dwarfs behave normally at low temperatures again suggests that the low masses obtained for the cool DA and DC white dwarfs in our sample are most likely related to problems with the physics of pure-H model atmospheres.

Figure 15 includes 47 IR-faint white dwarfs, which all show strong collision-induced absorption by molecular hydrogen in the near-infrared, 43 of which are in common with the analysis of Bergeron et al. (2022). Many of these appear to define the cool edge of our sample at all masses, and in particular in the upper right corner of the M versus T_{eff} diagram. The two DZ stars in the same region of the diagram are J1922+0233 and J2317+1830, also IR-faint white dwarfs (see Section 3.6). There is also one massive DC star overlapping this region, J1305+7022. Unfortunately, only Pan-STARRS *grizy* photometry is available, but our excellent fits with pure H or pure He models suggest that this is probably not an IR-faint white dwarf. As discussed at length in Bergeron et al. (2022), the coolest and most massive IR-faint white dwarfs in Figure 15 are found in the Debye cooling phase, when the specific heat decreases quickly with cooling, thus rapidly depleting the reservoir of thermal energy and producing the extreme increase of the cooling rate observed in the

upper right corner of Figure 15. To better illustrate this phenomenon, we indicated by a dotted curve the so-called Debye cooling phase, i.e., the rapidly cooling phase resulting from the transition, in the solid phase, from the classical regime where the specific heat of a solid is independent of temperature, to the quantum regime where it goes down from that constant value with decreasing temperature. As described in Bergeron et al. (2022), we define this transition from the classical to the quantum regime by isolating the evolving model where the central temperature becomes equal to $1/20$ the central Debye temperature ($\theta_D/T = 20$), as defined in Althaus et al. (2007). Only a dozen or so objects in our sample have reached the Debye cooling phase. We also emphasize that the presence of cool, IR-faint white dwarfs in this particular cooling phase is the direct result of the improved model atmospheres described in Bergeron et al. (2022), which led to higher T_{eff} and M values.

4.2 Low-Mass White Dwarfs

We now focus our attention towards the low-mass ($M < 0.45 M_{\odot}$) white dwarfs in Figure 15, which include mostly DA stars, but also several DQ, DZ, and DC white dwarfs. We consider each of the non-DA spectral types in turn.

One of the DZ stars is J1824+1212, also an IR-faint white dwarf with an extremely low temperature of $T_{\text{eff}} = 3381$ K (and $M = 0.346 M_{\odot}$), where the physics of our model atmospheres is most uncertain. The other DZ star is J0045+1420, a problematic object in our sample, probably magnetic, with an energy distribution that is not well reproduced by our models. The low masses inferred for these two DZ white dwarfs are thus uncertain.

Among the low-mass DQ white dwarfs, we already discussed in Section 3.4 the four DA + DQ unresolved binaries in our sample. To go further, we show in Figure 16 the carbon abundance as a function of effective temperature for all DQ white dwarfs in our sample, with these four binaries displayed in blue (all of these have $M < 0.3 M_{\odot}$), while the remaining DQs with $M < 0.45 M_{\odot}$ are shown in red. Three of these binaries have C abundances near the bottom of the envelope defining the DQ sequence, as expected if there is a companion that dilutes the strength of the carbon Swan bands, resulting in C abundances being underestimated (the other DA + DQ system above the sequence is J0613+2050, an extreme case of contamination by a DA component). We note that other low-mass DQ stars in our sample have carbon abundances near the bottom of the envelope (red symbols in Figure 16), suggesting that these may also be unresolved double degenerates, but this time composed of a DQ white dwarf and a featureless DC component. The only exception is J1501+2100 ($M = 0.248 M_{\odot}$), with a large carbon abundance above the sequence. Perhaps in this case there is indeed a low-mass DQ white dwarf in the system, dominating the luminosity, with a C abundance higher than average, which is expected in low-mass DQ white dwarfs, as discussed in Bédard et al. (2022b). Given these results, we inspected closely our fits to all low-mass DC white dwarfs and discovered that J0822+2023 ($M = 0.349 M_{\odot}$) shows a weak absorption band near 5150 \AA , indicating that this is probably an unresolved DQ + DC system as well.

With little evidence for low-mass single DQ white dwarfs, we examined the remaining low-mass ($M < 0.45 M_{\odot}$) DC stars in our sample, but this time by restricting our inspection to $T_{\text{eff}} > 5500$ K where the photometric analysis is less problematic. We find only 11 DC stars, three of which have no spectra available to us, and the spectral classification is thus difficult to confirm. A few of the remaining DCs have M-dwarf companions with bad photometric fits (see, e.g., J0200+1222 with $M = 0.217 M_{\odot}$), while in some cases, we can even

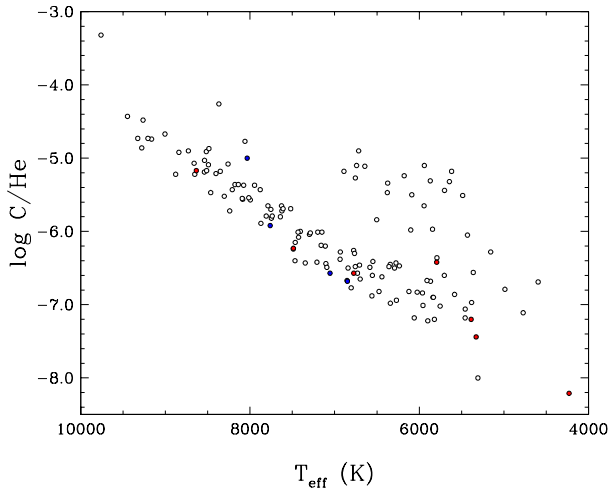


Figure 16. Carbon abundance as a function of effective temperature for all DQ white dwarfs in our sample. Coloured symbols all have $M < 0.45 M_{\odot}$, with the blue dots representing the four unresolved DA + DQ double degenerate systems.

detect a hint of $H\alpha$ (see J1325+4523), although the spectrum is rather noisy. Similarly, J1047+0007 ($M = 0.245 M_{\odot}$) appears to show Zeeman splitting at $H\alpha$ and could be magnetic. Hence, although we cannot completely rule out the existence of low-mass He-atmosphere white dwarfs in our sample, evidence suggests that most, if not all low-mass objects in our sample have hydrogen atmospheres. This result agrees with the conclusions of [Genest-Beaulieu & Bergeron \(2019b\)](#) who showed that there is no evidence for low-mass single DB white dwarfs, as determined from spectroscopy; several DB + DB systems have been identified by photometry, however, but these are probably composed of normal mass DB white dwarfs.

4.3 The Evolution of DA White Dwarfs

According to the analysis of [Bédard et al. \(2020\)](#), about 75% of all white dwarfs retain thick H layers and remain DA stars throughout their evolution. Hence a significant fraction of the DA white dwarfs in Figure 15 should remain DA stars in the temperature range displayed here, and eventually evolve into H-atmosphere DC stars at low temperatures when $H\alpha$ disappears. We can see that the coolest DA stars indeed merge with the cool DC sequence near $T_{\text{eff}} \sim 5000$ K, giving support to the idea that most cool DC stars in our sample have H-dominated atmospheres. Note also that in the temperature range considered in our analysis, it is possible for some of the DA stars to turn into He-rich DA or DC white dwarfs as a result of convective mixing. We come back to this point below.

What is particularly noteworthy in Figure 15 is the evolution of the crystallization sequence as a function of mass and T_{eff} . The mass distribution of DA white dwarfs displayed in Figure 13 of [Kilic et al. \(2020\)](#), based on spectroscopically confirmed DA stars hotter than 6000 K in the 100 pc sample and the SDSS footprint, shows a very strong peak at $\sim 0.6 M_{\odot}$, and a smaller but very broad shoulder centred at $\sim 0.8 M_{\odot}$ (see also Section 4.5 below). However, the results displayed in Figure 15 indicate that at $T_{\text{eff}} \sim 9000$ K, say, nearly half of the DA stars lie within the crystallization boundaries near $1.0 M_{\odot}$. As we go down in temperature, crystallization occurs at lower masses, until the crystallization sequence merges with the normal mass DA white dwarfs around 5500 K or so. Consequently,

when the cumulative mass distribution is considered (N versus M), the normal mass white dwarfs accumulate in the mean peak, while the crystallized DA stars are smeared out over this broad shoulder.

With the exception of a few objects, most white dwarfs above $0.9 M_{\odot}$ are DA stars, down to $T_{\text{eff}} \sim 5500$ K, below which they seem to evolve into He-rich IR-faint white dwarfs. The obvious mechanism responsible for this transformation is convective mixing. However, as discussed at length in [Bergeron et al. \(2022\)](#), the small H/He abundance ratios measured in these IR-faint white dwarfs ($\log H/He = -4$ to -3) imply that the total amount of hydrogen in these stars is extremely small, such that mixing should have occurred at higher temperatures ($T_{\text{eff}} \sim 9000$ K). Consequently, their immediate progenitors should be massive DC white dwarfs instead of DA stars. Two possible explanations are that the H abundance measured in these IR-faint white dwarfs is erroneous, or our understanding of convective mixing needs to be revised.

4.4 Magnetic White Dwarfs

Before discussing the evolution of He-atmosphere white dwarfs, it is worth investigating the magnetic objects in our sample and the role played by magnetism in the spectral evolution of these stars. Around 5% of the white dwarfs in our sample show signs of magnetism, whether it is through Zeeman splitting or polarization measurements. It is also detected in all spectral types (DA, DZ, DQ, DC); in the case of DQ white dwarfs, the strong C_2 Swan bands appear to be strongly shifted towards shorter wavelength. Various scenarios have been invoked to explain the origin of magnetic fields in white dwarfs (see the review by [Ferrario et al. 2015](#)), including a fossil origin, whether it was present in the forming stellar cloud or generated by a dynamo effect in rotating cores in the main sequence progenitor ([Angel et al. 1981](#); [Tout et al. 2004](#); [Wickramasinghe & Ferrario 2005](#); [Ferrario et al. 2015](#)). There is also strong evidence that binary evolution is responsible for producing magnetic fields in some white dwarfs (see, e.g., [Tout et al. 2008](#); [García-Berro et al. 2012](#)). More recently, it has also been proposed that the onset of core crystallization in cooling white dwarfs might produce magnetic fields through a dynamo process triggered by the onset of convection in the liquid core due to phase separation ([Isern et al. 2017](#); [Schreiber et al. 2021](#); [Ginzburg et al. 2022](#)). It thus appears that several mechanisms for producing magnetic fields might be at play here, which probably vary as a function of mass and cooling age (see Figure 2 of [Bagnulo & Landstreet 2022](#)), or equivalently, as a function of decreasing effective temperature.

We show in Figure 17 the same M versus T_{eff} diagram as in Figure 15 but this time by highlighting with red symbols the magnetic white dwarfs in our sample. Our results conclusively demonstrate that the presence of a magnetic field in most, if not all white dwarfs in our sample is strongly correlated with the phenomenon of core crystallization, as showed by the two blue solid curves, where the lower curve indicates the onset of crystallization at the centre of evolving models, while the upper one indicates the locations where 80% of the total mass has solidified. Note that the number of magnetic white dwarfs at low temperatures is most likely underestimated given the difficulty of detecting Zeeman splitting in weak $H\alpha$ absorption features. The situation is even worse in the case of DC stars, which would require spectropolarimetric measurements (e.g., [Putney 1997](#); [Bagnulo & Landstreet 2021](#); [Berdyugin et al. 2022](#)).

It has long been suggested that convective energy transport in cool white dwarfs ($T_{\text{eff}} \lesssim 10,000$ K) could be seriously impeded by the presence of a strong magnetic field. [Tremblay et al. \(2015\)](#) reexamined this problem using radiation magnetohydrody-

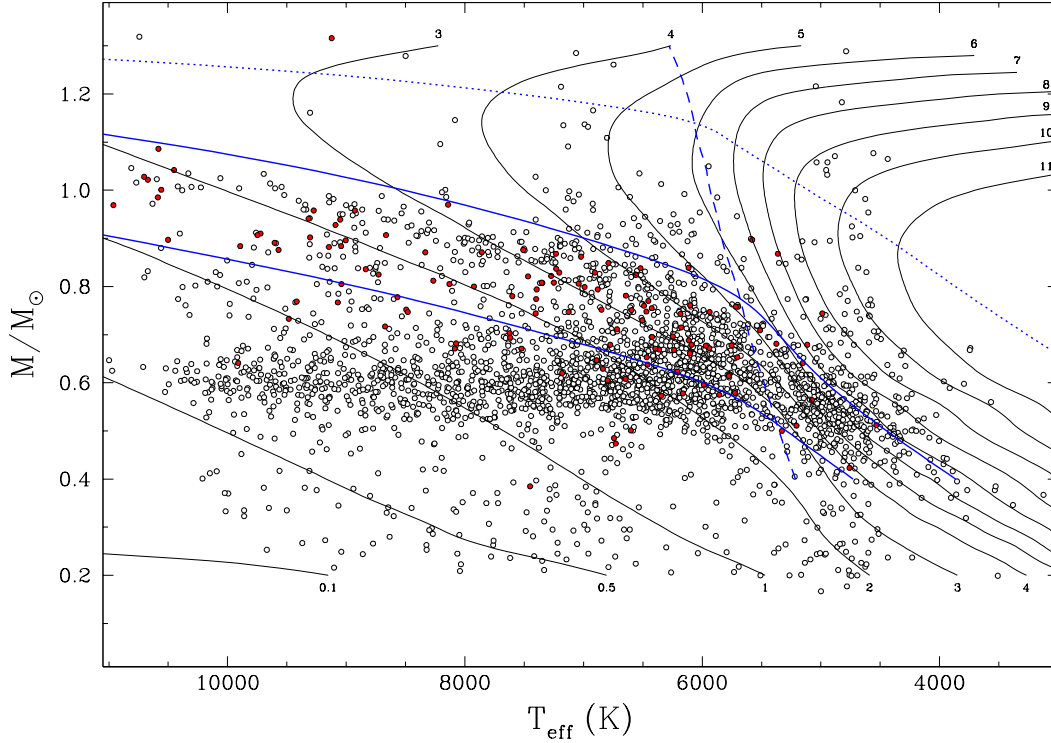


Figure 17. Same as Figure 15 but with magnetic white dwarfs shown as red dots (non-magnetic white dwarfs are shown with lighter circles to emphasize the magnetic objects).

dynamic simulations and indeed showed that magnetic fields of only tens of kG could significantly reduce the importance of convection to the point that the atmospheres become radiative. Model atmosphere analysis of magnetic white dwarfs can in principle be used to validate this finding by testing whether consistent fits can be obtained with non-convective atmospheres, but conflicting results have been reported (Lecavalier-Hurtubise & Bergeron 2017; Gentile Fusillo et al. 2018). In any case, magnetic fields can plausibly inhibit (at least partially) convective transport and this may be the key physical mechanism responsible for turning He-atmosphere white dwarfs into H-atmosphere white dwarfs at low temperatures, a question we investigate in the next subsection.

4.5 The Evolution of He-atmosphere White Dwarfs

We first reexamine the M versus T_{eff} diagram displayed in Figure 15, but this time, instead of differentiating the white dwarfs in terms of their spectral type, we separate them in terms of their main atmospheric constituent, H or He. The results are displayed in Figure 18. Also indicated by small dots in this figure are the 5358 white dwarf candidates (i.e. without spectral classification) found in the MWDD, and analysed under the assumption of a pure H composition for all objects. We remind the reader that there are only 2880 spectroscopically confirmed white dwarfs in our 100 pc sample, hence less than 35% of the total sample.

He-atmosphere white dwarfs in our sample may have different origins. First, their immediate progenitors could be DB stars. In this case, it has been shown that as they cool off, the bottom of the He convection zone can reach deep into the interior where resides a massive hydrogen reservoir, resulting into traces of H being brought up to the

surface, and thus producing a DBA star (Rolland et al. 2020, Bédard et al. 2022, submitted to ApJ). In some cases, however, there may be not enough hydrogen in the deep interior that the DB white dwarf retains a H-free atmosphere throughout its evolution. This particular channel is believed to be responsible for the origin of most DQ white dwarfs, while DQ stars with traces of hydrogen, such as those analysed in our study, are probably the result of convectively mixed DA stars below $T_{\text{eff}} \sim 12,000$ K (Bédard et al. 2022b). Convective mixing has also been invoked to account for the existence of the He-rich DA stars in our sample, as well as those reported in Rolland et al. (2018). Similarly, He-atmosphere DZ and DZA white dwarfs may descend from DB stars, or from convectively mixed DA stars. Finally, as discussed in Section 3.7.2, featureless DC white dwarfs must contain some traces of hydrogen, otherwise their masses inferred from photometry are too large; if they are devoid of hydrogen because of their prior evolution, it is believed they will become DQ white dwarfs instead. Thus, with the exception of some DQ stars, we expect the vast majority of cool, He-atmosphere white dwarfs to contain residual amounts of hydrogen in their atmosphere and stellar envelope. This is obviously the case for IR-faint white dwarfs as well.

Going back to the results displayed in Figure 18, we must remember that a pure H composition was assumed for all DC stars below $T_{\text{eff}} = 5200$ K. It is thus not a firm determination, but by far the most reasonable assumption given the results of our analysis. Indeed, as discussed in Section 2.3, such a sudden decrease of He-atmosphere white dwarfs in this temperature range is entirely consistent with the abrupt termination of the more luminous sequence of DC stars observed in the colour-magnitude diagram displayed in Figure 1. Given the location of this transition exactly in the range of mass and temperature where crystallization occurs, and given the correlation

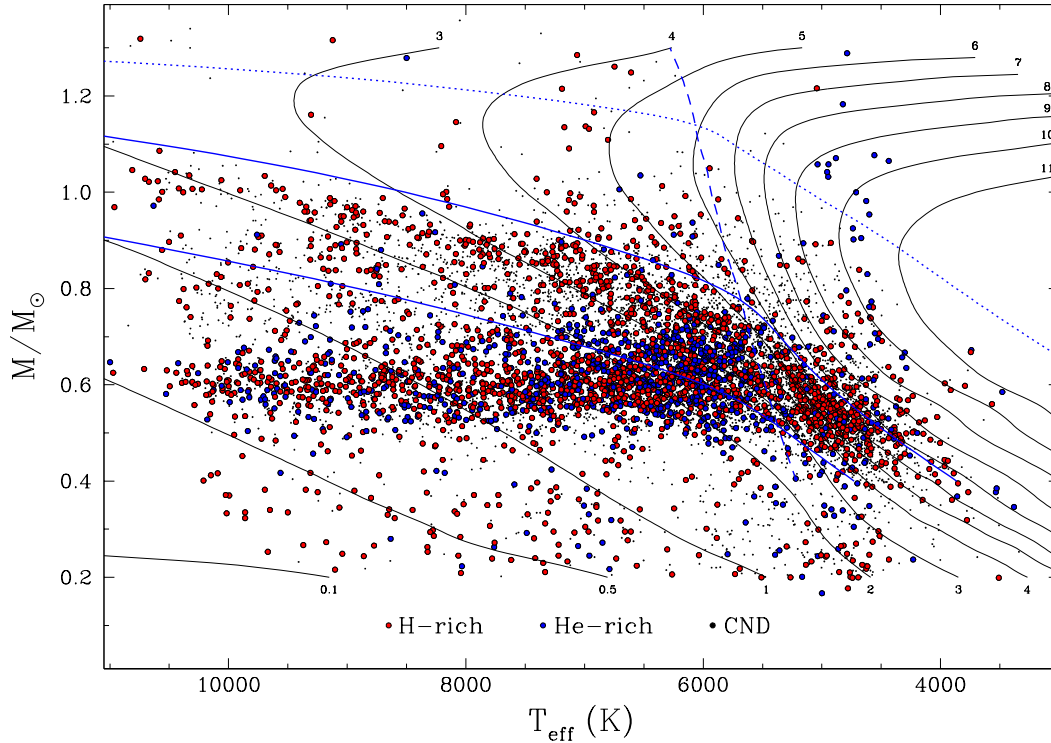


Figure 18. Same as Figure 15 with the exception that the objects are divided into H-atmosphere and He-atmosphere white dwarfs, as indicated in the legend. Also shown as small dots are the 5358 white dwarf candidates (without spectral classification) analysed under the assumption of a pure H composition.

between the occurrence of magnetism and crystallization discussed in Section 4.4, it is tantalizing to suggest that the mechanism responsible for transforming most, but not all, He-atmosphere white dwarfs into H-atmosphere white dwarfs is the following sequence of events: First, crystallization occurs in the stellar core and the crystallization front moves outward as the white dwarf cools off. This process eventually creates a magnetic field through the dynamo mechanism described in [Isern et al. \(2017\)](#). Then, the presence of the magnetic field suppresses completely, or even partially, convective transport, allowing the hydrogen thoroughly diluted within the mixed H/He convective envelope to diffuse upward, gradually building a thick H layer sitting on top of a deeper He-rich envelope. While detailed evolutionary calculations are required to explore this suggestion more quantitatively, this is certainly the most promising explanation for the transition from He-atmosphere to H-atmosphere white dwarfs that occurs below $T_{\text{eff}} = 5200$ K in Figure 18. Within this scenario, the few remaining cool ($T_{\text{eff}} \lesssim 5000$ K) He-atmosphere white dwarfs identified in our survey, most of which are DZ stars, could be interpreted as objects with not enough hydrogen, or no hydrogen at all.

We now consider the peak of the mass distribution at $\sim 0.6 M_{\odot}$ in Figure 18, but above $T_{\text{eff}} = 6000$ K where we can easily identify DA stars. In Figure 15, we already noticed that both the DQ and DZ white dwarfs had very narrow mass distributions, but that the DQ sequence had a lower mean mass than the DZ counterpart, while the DC stars appear to share the same mass distribution as DZ white dwarfs. But if we now compare the mass distributions of H-atmosphere and He-atmosphere white dwarfs in the same temperature range, displayed in Figure 18, we notice that they are remarkably similar. We can explore this more quantitatively by looking at the cumulative mass

distributions, N versus M , displayed in Figure 19, where we compare the mass distribution for the H-atmosphere DA stars above 6000 K with that for the He-atmosphere non-DA stars. For the latter, we also show the individual contributions from DC, DQ, and DZ white dwarfs. With the exception of the very broad shoulder observed for DA stars centred near $\sim 0.8 M_{\odot}$ and already discussed in Section 4.3, we notice that the mass distributions of H- and He-atmosphere white dwarfs are indeed remarkably similar, although there are obviously more DA stars in the central peak at $0.6 M_{\odot}$, probably originating from the evolutionary channel consisting of white dwarfs retaining thick H layers throughout their cooling history ($\sim 75\%$ of the entire white dwarf population according to [Bédard et al. 2020](#)).

Given the results shown in Figure 19, is it possible that the non-DA stars form a more homogeneous population than previously believed? First, as discussed in [Bédard et al. \(2022b\)](#), carbon can be more easily detected in lower mass DQ white dwarfs since the deep carbon diffusion tail sinks less rapidly in objects with lower surface gravity. Second, [Blouin \(2022\)](#) demonstrated that the simultaneous presence of metals at the photosphere of DQ white dwarfs can change the atmospheric structure significantly, to the point that carbon features vanish, thus explaining the paucity of DQZ white dwarfs. This could partially explain the near absence of an overlap between the mass distributions of DQ and DZ white dwarfs, as observed in both Figures 15 and 19. Finally, given that DC and DZ white dwarfs probably differ only by the presence of surrounding material being accreted, it is then possible that a significant fraction of DC stars also result from the evolution of this so-called PG 1159–DO–DB–DQ scenario (see [Bédard et al. 2022b](#) and references therein), and that only a small fraction of non-DA stars above 6000 K originate from convectively mixed DA white dwarfs.

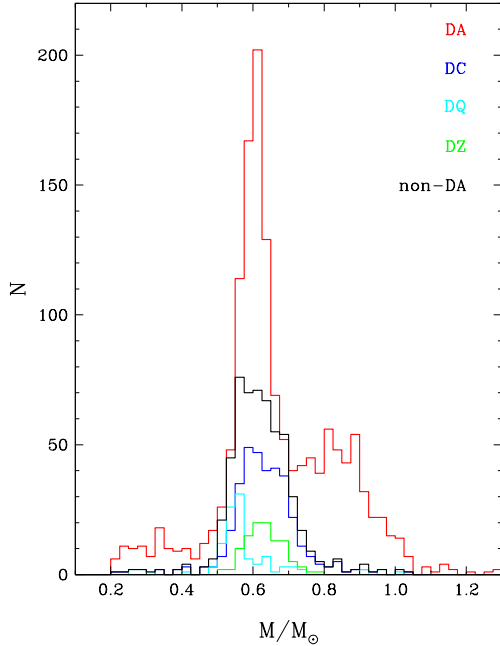


Figure 19. Mass distributions of all white dwarfs above $T_{\text{eff}} = 6000$ K split into different spectral types, as indicated in the legend. The black histogram represents the sum of all non-DA types (DC, DQ, DZ).

Although our sample is not statistically complete in any sense, we can still test this last hypothesis by looking at the variation of the fraction of He-atmosphere white dwarfs as a function of T_{eff} , the results of which are displayed in Figure 20. Surprisingly, despite the ill-defined statistical properties of our sample, our results are entirely consistent with those displayed in Figure 8 of McCleery et al. (2020), which are based on the volume-limited 40 pc sample in the northern hemisphere. First, we can see that above $T_{\text{eff}} \sim 6500$ K, the fraction of He-atmosphere white dwarfs remains nearly constant around 25%, which suggests that there is little evidence for convective mixing of DA white dwarfs into non-DA stars, at least not in the range of T_{eff} considered in our analysis. The situation changes drastically at lower temperatures, however, where the fraction increases to $\sim 45\%$ around 6500 K, and gradually decreases to 15% around 4000 K. We have to be careful, however, not to overinterpret our results at very low T_{eff} values because this is the range of temperature where our spectrophotometric analysis is most uncertain, and also because this is where the fraction of white dwarf candidates (i.e., not spectroscopically confirmed) is the largest. Indeed, from the results displayed in Figure 18, we estimate that above 6000 K, 40% of our total sample of objects are spectroscopically confirmed white dwarfs, while this fraction drops to $\sim 25\%$ below this temperature.

We thus conclude from the above discussion that convective mixing occurs in DA white dwarfs, but mostly at low effective temperature. In turn, this implies that most DA stars in the temperature range considered in our analysis have thick hydrogen layers around $\log q(\text{H}) \sim -7.5$ (at $M = 0.6 M_{\odot}$) according to the results displayed in Figure 19 of Bergeron et al. (2022), which explores the expected variation of the H/He ratio as a function of T_{eff} for DA models with various hydrogen layer masses.

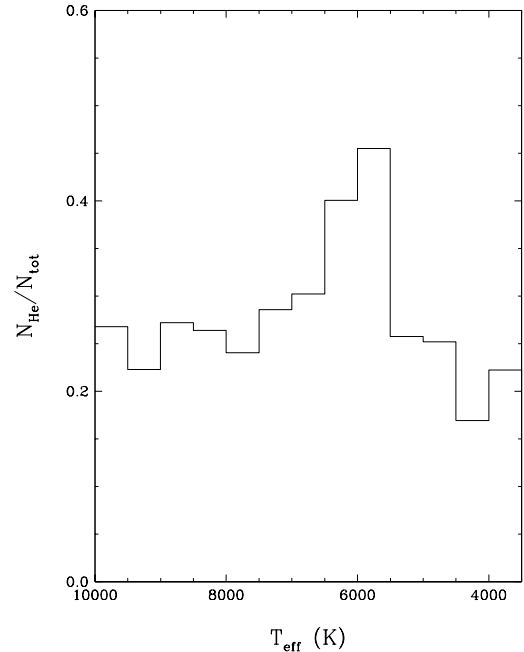


Figure 20. Ratio of He-atmosphere white dwarfs to the total number of stars as a function of effective temperature.

5 CONCLUSIONS

We selected 8238 white dwarfs and white dwarf candidates from the MWDD within 100 pc from the Sun and below $T_{\text{eff}} \sim 10,000$ K, 2880 of which were spectroscopically confirmed degenerates (35% of the sample). Optical and infrared photometry as well as spectroscopic observations, when available, were combined to measure the stellar parameters for each individual white dwarf in our sample using state-of-the-art model atmospheres appropriate for each spectral type. We can draw the following conclusions from our analysis:

1. There is now strong evidence that most, but probably not all, cool DC white dwarfs have H atmospheres. This conclusion is supported not only by the location of these objects in colour-magnitude diagrams, but also from our detailed photometric analysis. Effective temperature and stellar masses inferred from He-atmosphere models are unrealistically too low. However, our analysis has also revealed problems with the pure H model atmospheres, both in colour-magnitude diagrams and photometric fits, which we attributed to inaccuracies in the calculations of opacity sources, whether it is the red wing of $L\alpha$, the H^- bound-free opacity, or the CIA opacity from molecular hydrogen.

2. There is a more luminous observed sequence of DC white dwarfs in colour-magnitude diagrams that terminates around $T_{\text{eff}} \sim 5200$ K. Our detailed photometric analysis suggests that below this temperature, He-atmosphere white dwarfs turn into H-atmosphere white dwarfs. The mechanism by which this transformation occurs appears to be related to the onset of crystallization and to the occurrence of magnetism being generated as a result of this process. The presence of a magnetic field would lead to a suppression, even partially, of convective transport, allowing hydrogen, thoroughly diluted within the deep stellar envelope, to float back to the surface.

3. Some DQ white dwarfs show traces of hydrogen in the form

of an $H\alpha$ absorption feature. In some cases, these are obviously unresolved DA + DQ binaries (due in part to their overluminosity), but other objects are genuine DQA stars, most likely originating from convectively mixed DA stars. We believe that we may also have identified a population of cool DQ white dwarfs in which the presence of hydrogen manifests itself as collision-induced absorption by molecular hydrogen in the near-infrared, although a more detailed analysis using model atmospheres including H, He, and C is required to confirm this interpretation.

4. We identified several unresolved double degenerate binaries in our sample, all of which have been analyzed under the assumption of a single object. These systems deserve further study to deconvolve the stellar parameters of the individual components, following the approach described in Bédard et al. (2017).

5. Our analysis reveals that most low-mass white dwarfs probably have H atmospheres, which would in turn indicate that common-envelope evolution most likely produces white dwarf remnants that retain thick H layers.

6. The mass distributions of DQ, DZ, and DC white dwarfs suggest that these may form a more homogeneous population than previously believed, with the DQ stars representing the low-mass component of the non-DA white dwarfs, in which carbon features can be more easily detected. Carbon features would be more difficult to detect in DZ and DC white dwarfs due to their higher mass and/or larger metal content. If this is indeed the case, it is possible that a larger fraction of non-DA white dwarfs below $T_{\text{eff}} = 10,000$ K evolve from the so-called PG 1159–DO–DB–DQ scenario.

7. We found little evidence in our sample for the transformation of a large fraction of DA stars into He-atmosphere white dwarfs through the process of convective mixing between $T_{\text{eff}} = 10,000$ K and ~ 6500 K. The He-rich DA stars are the obvious exception, but there are very few of those in our sample (or even in the entire SDSS white dwarf sample for that matter, see Rolland et al. 2018).

8. We do, however, find evidence for convective mixing below $T_{\text{eff}} \sim 6500$ K, where the fraction of He-atmosphere white dwarfs increases to $\sim 45\%$, which suggests that most DA stars in the temperature range considered in our analysis have thick hydrogen layers around $\log g(\text{H}) \sim -7.5$.

9. Finally, there is an obvious need for more near-infrared photometry, with better accuracy and precision, required for the analysis of cool ($T_{\text{eff}} < 6000$ K) white dwarfs, in particular for the determination of the chemical composition, and in some cases even the main atmospheric constituent.

Our understanding of the spectral evolution of cool white dwarfs is like a giant puzzle, where individual pieces are added one by one in order to build a better picture, as better observational data and theoretical models become available over the years. We feel we have added a few pieces of that puzzle in our analysis, but the overall picture remains incomplete. Even though we are convinced that progress can only be accomplished through tailored analyses of individual objects in a given sample, we felt we have reached the limit of human capacity to analyse individually each object in such a large sample of nearly 3000 white dwarfs. Better techniques for handling bigger data sets involving machine learning algorithms will eventually become necessary.

ACKNOWLEDGEMENTS

We are grateful to A. Bédard for enlightening discussions. This work was supported in part by NSERC Canada and by the Fund FRQ-NT

(Québec). SB is a Banting Postdoctoral Fellow and a CITA National Fellow, supported by NSERC.

Funding for the Sloan Digital Sky Survey (<https://www.sdss.org>) has been provided by the Alfred P. Sloan Foundation, the U.S. Department of Energy Office of Science, and the Participating Institutions. SDSS-IV acknowledges support and resources from the Center for High-Performance Computing at the University of Utah, and is managed by the Astrophysical Research Consortium for the Participating Institutions of the SDSS Collaboration (Blanton et al. 2017).

This work has made use of data from the European Space Agency mission *Gaia* (<https://www.cosmos.esa.int/gaia>), processed by the *Gaia* Data Processing and Analysis Consortium (DPAC). Funding for the DPAC has been provided by national institutions, in particular the institutions participating in the *Gaia* Multilateral Agreement (*Gaia* Collaboration et al. 2018a).

This research has also made use of the NASA Astrophysics Data System Bibliographic Services; the Montreal White Dwarf Database (Dufour et al. 2017); the SIMBAD database, operated at the Centre de Données astronomiques de Strasbourg (Wenger et al. 2000); and the NASA/IPAC Infrared Science Archive, operated at the California Institute of Technology.

DATA AVAILABILITY

The astrometric, photometric and spectroscopic data underlying this article are available in the MWDD at <http://www.montrealwhitedwarfdatabase.org>. The astrometric and photometric data are also available as online supplementary material.

REFERENCES

- Allard N. F., Kielkopf J. F., 2009, *A&A*, **493**, 1155
 Althaus L. G., García-Berro E., Isern J., Córscico A. H., Rohrmann R. D., 2007, *A&A*, **465**, 249
 Angel J. R. P., Borra E. F., Landstreet J. D., 1981, *ApJS*, **45**, 457
 Bagnulo S., Landstreet J. D., 2021, *MNRAS*, **507**, 5902
 Bagnulo S., Landstreet J. D., 2022, *ApJ*, **935**, L12
 Bédard A., Bergeron P., Fontaine G., 2017, *ApJ*, **848**, 11
 Bédard A., Bergeron P., Brassard P., Fontaine G., 2020, *ApJ*, **901**, 93
 Bédard A., Brassard P., Bergeron P., Blouin S., 2022a, *ApJ*, **927**, 128
 Bédard A., Bergeron P., Brassard P., 2022b, *ApJ*, **930**, 8
 Berdyugin A. V., Pirola V., Bagnulo S., Landstreet J. D., Berdyugina S. V., 2022, *A&A*, **657**, A105
 Bergeron P., Wesemael F., Liebert J., Fontaine G., 1989, *ApJ*, **345**, L91
 Bergeron P., Saffer R. A., Liebert J., 1992, *ApJ*, **394**, 228
 Bergeron P., Ruiz M.-T., Leggett S. K., Saumon D., Wesemael F., 1994, *ApJ*, **423**, 456
 Bergeron P., Ruiz M. T., Leggett S. K., 1997, *ApJS*, **108**, 339
 Bergeron P., Leggett S. K., Ruiz M. T., 2001, *ApJS*, **133**, 413
 Bergeron P., Dufour P., Fontaine G., Coutu S., Blouin S., Genest-Beaulieu C., Bédard A., Rolland B., 2019, *ApJ*, **876**, 67
 Bergeron P., Kilic M., Blouin S., Bédard A., Leggett S. K., Brown W. R., 2022, arXiv e-prints, p. [arXiv:2206.03174](https://arxiv.org/abs/2206.03174)
 Blanton M. R., et al., 2017, *AJ*, **154**, 28
 Blouin S., 2022, *A&A*, **666**, L7
 Blouin S., Dufour P., 2019, *MNRAS*, **490**, 4166
 Blouin S., Xu S., 2022, *MNRAS*, **510**, 1059
 Blouin S., Kowalski P. M., Dufour P., 2017, *ApJ*, **848**, 36
 Blouin S., Dufour P., Allard N. F., 2018a, *ApJ*, **863**, 184
 Blouin S., Dufour P., Allard N. F., Kilic M., 2018b, *ApJ*, **867**, 161
 Blouin S., Dufour P., Thibeault C., Allard N. F., 2019, *ApJ*, **878**, 63

- Casewell S. L., Debes J., Braker I. P., Cushing M. C., Mace G., Marley M. S., Kirkpatrick J. D., 2020, *MNRAS*, **499**, 5318
- Chambers K. C., et al., 2016, arXiv e-prints, p. [arXiv:1612.05560](https://arxiv.org/abs/1612.05560)
- Coutu S., Dufour P., Bergeron P., Blouin S., Loranger E., Allard N. F., Dunlap B. H., 2019, *ApJ*, **885**, 74
- Dufour P., Bergeron P., Fontaine G., 2005, *ApJ*, **627**, 404
- Dufour P., et al., 2007, *ApJ*, **663**, 1291
- Dufour P., Blouin S., Coutu S., Fortin-Archambault M., Thibeault C., Bergeron P., Fontaine G., 2017, in Tremblay P. E., Gaensicke B., Marsh T., eds, *Astronomical Society of the Pacific Conference Series Vol. 509, 20th European White Dwarf Workshop*. p. 3 ([arXiv:1610.00986](https://arxiv.org/abs/1610.00986))
- Ferrario L., Melatos A., Zrake J., 2015, *Space Sci. Rev.*, **191**, 77
- Gaia Collaboration et al., 2018a, *A&A*, **616**, A1
- Gaia Collaboration Babusiaux C., van Leeuwen F. e. a., 2018b, *A&A*, **616**, A10
- Gaia Collaboration et al., 2022, arXiv e-prints, p. [arXiv:2208.00211](https://arxiv.org/abs/2208.00211)
- García-Berro E., et al., 2012, *ApJ*, **749**, 25
- Genest-Beaulieu C., Bergeron P., 2019a, *ApJ*, **871**, 169
- Genest-Beaulieu C., Bergeron P., 2019b, *ApJ*, **882**, 106
- Gentile Fusillo N. P., Tremblay P. E., Jordan S., Gänsicke B. T., Kalirai J. S., Cummings J., 2018, *MNRAS*, **473**, 3693
- Gentile Fusillo N. P., et al., 2019, *MNRAS*, **482**, 4570
- Gentile Fusillo N. P., et al., 2021, *MNRAS*,
- Giammichele N., Bergeron P., Dufour P., 2012, *ApJS*, **199**, 29
- Gianninas A., Bergeron P., Ruiz M. T., 2011, *ApJ*, **743**, 138
- Ginzburg S., Fuller J., Kawka A., Caiazzo I., 2022, *MNRAS*, **514**, 4111
- Greenstein J. L., 1986, *ApJ*, **304**, 334
- Hall P. B., Kowalski P. M., Harris H. C., Awal A., Leggett S. K., Kilic M., Anderson S. F., Gates E., 2008, *AJ*, **136**, 76
- Holberg J. B., Bergeron P., 2006, *AJ*, **132**, 1221
- Hollands M. A., Tremblay P. E., Gänsicke B. T., Gentile-Fusillo N. P., Toonen S., 2018, *MNRAS*, **480**, 3942
- Hollands M. A., Tremblay P.-E., Gänsicke B. T., Koester D., Gentile Fusillo N. P., 2021, *Nature Astronomy*, **5**, 451
- Hummer D. G., Mihalas D., 1988, *ApJ*, **331**, 794
- Iglesias C. A., Rogers F. J., Saumon D., 2002, *ApJ*, **569**, L111
- Isern J., García-Berro E., Külebi B., Lorén-Aguilar P., 2017, *ApJ*, **836**, L28
- Kawka A., Vennes S., Schmidt G. D., Wickramasinghe D. T., Koch R., 2007, *ApJ*, **654**, 499
- Kepler S. O., et al., 2019, *MNRAS*, **486**, 2169
- Kilic M., von Hippel T., Mullally F., Reach W. T., Kuchner M. J., Winget D. E., Burrows A., 2006, *ApJ*, **642**, 1051
- Kilic M., Bergeron P., Kosakowski A., Brown W. R., Agüeros M. A., Blouin S., 2020, *ApJ*, **898**, 84
- Kleinman S. J., et al., 2013, *ApJS*, **204**, 5
- Koester D., Voss B., Napiwotzki R., Christlieb N., Homeier D., Lisker T., Reimers D., Heber U., 2009, *A&A*, **505**, 441
- Kowalski P. M., Saumon D., 2006, *ApJ*, **651**, L137
- Kowalski P. M., Mazevet S., Saumon D., Challacombe M., 2007, *Phys. Rev. B*, **76**, 075112
- Lecavalier-Hurtubise É., Bergeron P., 2017, in Tremblay P. E., Gaensicke B., Marsh T., eds, *Astronomical Society of the Pacific Conference Series Vol. 509, 20th European White Dwarf Workshop*. p. 169
- Leggett S. K., et al., 2018, *ApJS*, **239**, 26
- Liebert J., Bergeron P., Holberg J. B., 2005, *ApJS*, **156**, 47
- Limoges M. M., Bergeron P., Lépine S., 2015, *ApJS*, **219**, 19
- Lindgren L., et al., 2018, *A&A*, **616**, A2
- Lindgren L., et al., 2021, *A&A*, **649**, A4
- López-Sanjuan C., et al., 2022, *A&A*, **658**, A79
- Magnier E. A., et al., 2013, *ApJS*, **205**, 20
- McCleery J., et al., 2020, *MNRAS*, **499**, 1890
- O'Brien M. W., et al., 2022, arXiv e-prints, p. [arXiv:2210.01608](https://arxiv.org/abs/2210.01608)
- Press W. H., Flannery B. P., Teukolsky S. A., 1986, *Numerical recipes. The art of scientific computing*. Cambridge University Press
- Putney A., 1997, *ApJS*, **112**, 527
- Rolland B., Bergeron P., Fontaine G., 2018, *ApJ*, **857**, 56
- Rolland B., Bergeron P., Fontaine G., 2020, *ApJ*, **889**, 87
- Saumon D., Holberg J. B., Kowalski P. M., 2014, *ApJ*, **790**, 50
- Saumon D., Blouin S., Tremblay P.-E., 2022, *Phys. Rep.*, **988**, 1
- Schreiber M. R., Belloni D., Gänsicke B. T., Parsons S. G., Zorotovic M., 2021, *Nature Astronomy*, **5**, 648
- Spiegelman F., Allard N. F., Kielkopf J. F., 2022, *A&A*, **659**, A157
- Tonry J. L., et al., 2012, *ApJ*, **750**, 99
- Tout C. A., Wickramasinghe D. T., Ferrario L., 2004, *MNRAS*, **355**, L13
- Tout C. A., Wickramasinghe D. T., Liebert J., Ferrario L., Pringle J. E., 2008, *MNRAS*, **387**, 897
- Tremblay P. E., Bergeron P., Gianninas A., 2011, *ApJ*, **730**, 128
- Tremblay P. E., Fontaine G., Freytag B., Steiner O., Ludwig H. G., Steffen M., Wedemeyer S., Brassard P., 2015, *ApJ*, **812**, 19
- Tremblay P. E., Cukanovaite E., Gentile Fusillo N. P., Cunningham T., Hollands M. A., 2019a, *MNRAS*, **482**, 5222
- Tremblay P.-E., et al., 2019b, *Nature*, **565**, 202
- Tremblay P. E., et al., 2020, *MNRAS*, **497**, 130
- Wenger M., et al., 2000, *A&AS*, **143**, 9
- Wickramasinghe D. T., Ferrario L., 2005, *MNRAS*, **356**, 1576
- Wickramasinghe D. T., Allen D. A., Bessell M. S., 1982, *MNRAS*, **198**, 473

This paper has been typeset from a $\text{\TeX}/\text{\LaTeX}$ file prepared by the author.